X-ray rocking curve and ferromagnetic resonance investigations of ion-implanted magnetic garnet

V. S. Speriosu and C. H. Wilts
California Institute of Technology, Pasadena, California 91125

(Received 3 December 1982; accepted for publication 7 February 1983)

Detailed analyses of x-ray rocking curves and ferromagnetic resonance spectra were used to characterize properties of ⟨111⟩-oriented Gd, Tm, Ga:YIG films implanted with Ne^+, He^+, and H_2^+. For each implanted species the range of doses begins with easily analyzed effects and ends with paramagnetism or amorphousness. Ion energies were chosen to produce implanted layer thicknesses of 3000 to 6000 Å. Profiles of normal strain, lateral strain, and damage were obtained. The normal strain increases with dose and near amorphousness is 2.5%, 3.4%, and 3.9% for Ne^+, He^+, and H_2^+, respectively. Lateral strain is 0 for all values of normal strain, implying absence of plastic flow. Comparison of these results with the reported decrease in lateral stress implies either a large reduction in Young's modulus or a transition to rhombohedral equilibrium unit cell. Damage is modelled by a spherically-symmetric Gaussian distribution of incoherent atomic displacements. Due to the use of (444), (888), and (880) reflections the sensitivity is greatest for the *c* sites occupied by Gd, Tm, and Y. The standard deviation of displacements increases linearly with strain with proportionality constant 0.25, 0.18, and 0.13 Å/% for Ne^+, He^+, and H_2^+, respectively. For maximum strains up to 1.3% annealing in air reduces the strain without changing the shape of the profile. The behavior of the strain with annealing is nearly independent of implanted species or doses. After annealing at 600 °C the strain is 40% of the original value. Magnetic profiles obtained before and after annealing were compared with the strain profiles. The local change in anisotropy field ΔH_k with increasing strain shows an initially linear rise for both He^+ and Ne^+. The slope is -4.1 kOe/%, in agreement with the magnetostriction effect estimated from the composition. For strain values between 1 and 1.5%, ΔH_k saturates reaching peak values of -3.6 kOe for He^+ and -2.8 kOe for Ne^+. At strain values near 2.3% for He^+ and 1.8% for Ne^+, ΔH_k drops to nearly 0 and the material is paramagnetic. For peak strains greater than 1.3% for He^+ and 1.1% for Ne^+ the relation between uniaxial anisotropy and strain is not unique. The saturation magnetization $4\pi M$, the ratio of exchange stiffness to magnetization (A/M) and the cubic anisotropy H_1 decrease with strain reaching 0 at 2.3% and 1.8% for He^+ and Ne^+, respectively. At these strain values the damping coefficient α is 50% and 80% greater than bulk value for He^+ and Ne^+, respectively. For higher observed strains the material remains paramagnetic. Upon annealing of samples implanted with low doses of Ne^+ and He^+ the anisotropy field follows uniquely the behavior with strain for unannealed material. At 600 °C the magnetization returns to bulk value but the ratio A/M remains 20% low. For H_2^+ implantation the total ΔH_k consists of a magnetostrictive contribution due to strain and of a comparable excess contribution associated with the local concentration of hydrogen. The profile of excess ΔH_k agrees with calculated LSS range. The presence of hydrogen results in a reduction of $4\pi M$ not attributable to strain or damage. For a peak strain of 0.60% and a peak total ΔH_k of -4.5 kOe, the magnetization is only 40% of bulk value. After annealing up to 350 °C the excess ΔH_k diminishes and redistributes itself to the regions neighboring the peak damage. At 400 °C the excess is nearly 0. For higher annealing temperatures the only component of ΔH_k is magnetostrictive. At 600 °C, the magnetization, the ratio A/M, and α return to bulk values.

PACS numbers: 75.30. − m, 61.10.Fr, 76.50. + g, 61.70.Tm

I. INTRODUCTION

Since the discovery[1] that ion-implantation in magnetic garnets is useful in the manufacture of devices, there has been an interest in the properties of implanted garnets. These properties may be subdivided into three broad categories: (1) the damage viewed primarily from a crystallographic point of view, (2) the possible effects due to the presence of the dopant, and (3) the magnetic properties arising from (1) and (2).

Damage has been studied by x-ray diffraction,[1–13] indirectly through stress measurements,[14–16] enhanced etch rate measurements,[17–19] Rutherford backscattering,[20–22] and electron diffraction.[23] Magnetic properties have been studied through the capping-layer effect,[2,4,24] ferromagnetic resonance (FMR),[25–32] ac susceptibility,[33] Mossbauer spectroscopy,[34,35] vibrating sample magnetometry,[9] and Kerr rotation.[36] Although no direct measurements of dopant distribution have been published, studies have been made of their anneal-induced desorption.[8]

 0021-8979/83/063325-19$02.40

One conclusion drawn from this work is that the strain and damage are uniquely related to the energy deposited through nuclear collisions.[1,37,38] Generally, no crystallographic effects are attributed to the presence of the dopant. Another conclusion drawn is that the major connection between changes in magnetic and crystalline properties is magnetostriction,[39] promoting efforts to measure the magnetostriction constant of virgin and implanted crystals.[40–42] An apparent lack of correlation between strain and uniaxial anisotropy H_k at high doses has led to the hypothesis that implantation destroys the growth-induced anisotropy.[43] Other effects include changes in the saturation magnetization M, in the exchange stiffness A, in the Curie temperature T_C, in the cubic anisotropy H_1, and in the damping parameter α.[9,11,13,31,32,43] In the case of H^+-implanted garnet the unusually large variation of uniaxial anisotropy with dose[44] and annealing[8,10] has been attributed to either (1) qualitatively different damage caused by H^+ implantation,[45] or (2) chemical effects due to the presence of H in the lattice.[8,10,46] Despite the relatively large number of papers devoted to implanted garnets, many of their basic features are unresolved. Part of this is due to difficulties of interpretation of experimental results and frequent failure to extract the maximum of quantitative information available in the experimental data.

In this paper we have combined x-ray diffraction and ferromagnetic resonance measurements of Ne^+, He^+, and H_2^+ implanted ⟨111⟩-oriented Gd, Tm, Ga:YIG. This choice of implanted species and host material was made because of their (previously) widespread use in the manufacture of devices. More important, this material has the beneficent properties of reasonably narrow linewidth and high magnetostriction (70 Oe and $\lambda_{111} \sim -3\times10^{-6}$). The narrow linewidth permits a clear identification of mode location and amplitude in FMR, while the large λ_{111} ensures that a relatively large number of modes are supported in the implanted layer, thereby providing data with high information content. For each implanted species, doses were chosen to cover a range starting with easily analyzed effects up to amorphousness. The incident ion energy produced implanted layer thicknesses of 3000–6000 Å. Selected samples were annealed up to 600 °C.

We have attempted to answer the following questions: (1) Can FMR and x-ray diffraction yield detailed and unequivocal information about magnetic and crystalline properties for all levels of damage? (2) If so, what is the extent of correlation between magnetic and crystalline properties? The answer to the first question is a qualified yes. Concerning the second question, there is a strong although not total correlation between measured magnetic and measured crystalline properties.

II. EXPERIMENT

The garnet used was LPE-grown, ⟨111⟩-oriented Gd, Tm, Ga:YIG. The substrate material was the usual single-crystal $Gd_3Ga_5O_{12}$ (GGG) wafer with a 5 cm diameter and 0.5 mm thickness. Two wafers with films of identical nominal composition and very similar bulk magnetic properties were used, one (M721) for the neon and helium implantations, and the other (M722) for the hydrogen implantations. Two nominally identical, 4×4 mm^2 samples were made for each implanted species and dose. Implantation was done at room temperature. (See Table I for details). These three series of implanted samples were provided to us by an external source.[47]

TABLE I. Some bulk properties of garnet and implantation schedule.

Nominal composition $\{Gd_{0.84}Tm_{1.17}Y_{0.99}\}[Fe_2](Ga_{0.39}Fe_{2.61})O_{12}$			
Nominal thickness (μm)		0.95	
$\lvert F_{444}\rvert$[a]		1074	
$\lvert F_{888}\rvert$		974	
$\lvert F_{880}\rvert$		1124	
μ_{abs} (μm^{-1})		0.117	
$4\pi M$ (Gauss)[b]		510	
Wafer	Ion	Nominal energy (keV)	Nominal dose (10^{13}/cm^2)
M721	Ne^+	190	5
			10
			20
			30
			50
M721	He^+	140	300
			600
			1200
			2000
M722	H_2^+	120	200
			300
			500
			2000
			4000
Implantation current density		0.25 μA/cm^2	

[a] Structure factors and normal absorption coefficient calculated from the composition.
[b] Calculated from magnetic bubble properties.

In the determination of magnetic profiles for high doses, it was found useful to chemically etch some of the neon and helium implanted samples. A 30 min preanneal in air at 150 °C produced no detectable changes in either FMR or x-ray diffraction. Following this, the sample was etched in hot (110 °C) H_3PO_4. After cleaning with organic solvents, the sample was plunged in the acid and stirred for 5 to 10 sec., followed by immersion in room temperature water. The sample was etched and measured with FMR or FMR and x-ray techniques in successive steps, up to the disappearance or near disappearance of the signal attributed to the implanted layer. The longest total etch time was 1 min. The amount of material removed was determined with an accuracy of about $\pm$ 50 Å from the x-ray rocking curve by inverting the process discussed in Ref. 7. Lateral nonuniformities attributed to uneven etching were detected by the broadening of both the FMR absorption spectrum and the rocking curve. The broadening increased with successive etch steps, but did not impair the x-ray determination of layer thickness. In the case of FMR, the broadening at the last two etch steps vitiated a meaningful measurement of some surface mode amplitudes, reduced the sensitivity for detection of weak modes, and in-

creased the uncertainty in surface mode location from the usual ± 5 Oe (unetched) up to ± 150 Oe (last etch step). Other than nonuniform etching of the surface, we found no evidence of etch-induced changes in either crystalline or magnetic profiles. Selected unetched samples were annealed in air at temperatures ranging from 150 to 600 °C in steps of 50 °C. Due to the limited supply of samples, the same sample was annealed at progressively higher temperature in successive steps lasting 30 min each. FMR measurements were made every 50 °C, while rocking curves were taken every 100 °C.

Double crystal, Bragg case, x-ray rocking curves were taken under the conditions described in Ref. 7. The x-ray source line was Cu Kα with an incident beam counting rate of 10^5 cps. The spot size at the sample was limited to $\sim 1 \times 1$ mm^2 by a set of slits. All as-implanted samples were measured using the (444) reflection. In certain cases described below, the (880) $\gamma_0 > |\gamma_H|$, and the (880) $\gamma_0 < |\gamma_H|$, reflections were also used. For the annealed samples, especially for annealing temperatures greater than 350 °C, the (888) reflection was used because of its sensitivity to low strain. Measurements repeated up to several months apart produced practically identical rocking curves.

Ferromagnetic resonance measurements were made at a fixed frequency of 9.5 GHz with the usual combination of rectangular cavity, microwave bridge, and modulated external applied field. All measurements were made at room temperature without a temperature controller. Both perpendicular and parallel FMR configurations were used for each sample. For some samples FMR spectra as a function of polar angle were also taken. The reproducibility of mode location and amplitude determination was ± 5 Oe and $\pm 2\%$, respectively, for measurements repeated within a few hours. However, spectra taken several days apart at times showed systematic differences up to 50 Oe in mode location, without appreciable changes in mode amplitude. We attribute these variations to differences in room temperature, since one can observe shifts of several hundred Oe by blowing warm ($T \sim 50$ °C) air into the cavity. We do not consider the observed variations to be significant since the range of applied field in which the modes are excited spans several thousand Oe.

III. THEORETICAL CONSIDERATIONS

It is perhaps inappropriate to include here a qualitative description of the basic processes of ion implantation. The major purpose of this paper is to present experimental results. However, the impression formed by reading the literature on ion-implanted garnets is that different authors assign different meanings to the same words. At the risk of belaboring the point, we wish to give a precise description of what we think we are measuring.

During ion-implantation the incident ions undergo collisions with target atoms. Since the ion beam is aimed in a nonchanneling direction, the crystallographic structure of the target plays only a minor role in determining the scattering process. The parameters which enter the expression for this process are the masses and nuclear charges of the ion and target atoms, the density (number of each kind of atom per unit volume) of the target, its electronic density, and the kinetic energy of the ion beam.[48] Since the ions continuously lose energy as they penetrate the crystal, the energy dependence becomes at least statistically a depth dependence. Due to the low electron mass, collisions with electrons remove energy but do not contribute to damage.[48] For typical implantation in garnet at a few hundred keV, the number of nuclear collisions per ion is several hundred.[45] At each collision the transferred energy ranges from zero up to a value determined by the kinetic energy of the ion and the ion-target mass ratio. If the transferred energy is sufficiently large, the target atom will be ejected from its original site and may in turn eject other atoms. Thus for each incoming ion there is a cascade of recoil atoms (a thermal spike). The mean free path of the ion is sufficiently short,[45] so that even for the lowest doses we are considering ($\sim 10^{13}$/cm^2 for Ne^+ and $\sim 10^{15}$/cm^2 for He^+ and H_2^+), at least one atom from almost every unit cell has been displaced by more than one interatomic spacing. Atoms surrounding either the vacancy or the interstitial atom are no longer located in perfect crystal sites. Since an interstitial and a vacancy are not equivalent, it is plausible that in the implantation region the atoms are no longer packed as closely as in virgin crystal. This is the positive strain uniformly observed in ion-implanted crystals with widely different properties, such as Si, GaAs, and GGG.[7,49]

If the displacement of a particular atom j is $\Delta \mathbf{r}_j$, then there is a probability distribution $\rho(\Delta \mathbf{r}_j)$ which describes the frequency of these incoherent displacements. For a polyatomic crystal, such as garnet, one expects that each set of equivalent sites, occupied by a particular atomic species, has its own $\rho(\Delta \mathbf{r}_j)$, each contributing in a different way to the total (coherent) strain. For ion doses below that required to render the crystal amorphous, the unit cell is still recognizable. The registry between the implanted layer and the underlying undamaged crystal is maintained. It constrains the average unit cell to expand only in a direction perpendicular to the film surface.[7] The implanted layer is therefore in lateral compression and the total normal strain includes a Poisson (elastic) contribution. The compressive stress may act as a source of energy for the creation of extended defects. If the stress is sufficiently large, stress-reducing dislocations may form.[50] Such an occurrence is accompanied by the loss of strict registry between highly stressed and less stressed regions of the crystal.

Up to now we have not considered any crystallographic effects due to the presence of the implanted dopant. Although *a priori* it is not possible to exclude the dopant as a contributor to the total strain, experimental results strongly suggest that only the damage is effective. For the same strain, the doses for neon versus helium differ by one and a half orders of magnitude,[1,38] conforming to the difference in nuclear stopping power. The hypothesis that damage is the source of the strain is further confirmed in Ref. 38, where the detailed strain distribution was found to agree closely with the calculated distribution of energy deposited in nuclear collisions, but not with the ion range. Our present results, discussed below, suggest that in the case of hydrogen im-

plantation there is a detectable strain associated with the ion range.

X-ray diffraction can detect and separate the implantation-induced damage components: point defects, strains, and extended defects. Point defects change the value of the structure factor. If they are incoherent, the magnitude of the structure factor is diminished. This decrease is determined by the displacement functions $\rho(\Delta \mathbf{r}_j)$ belonging to each site j. We make the simplifying and physically plausible assumption that these functions are spherically symmetric Gaussians described by their standard deviations U_j. A further simplification is that, at a given depth, $U_j \equiv U$ is the same for all sites. For the reflections used in this work, the c-sites, occupied by Gd, Tm, and Y, are the dominant contributors to the structure factor. Thus the experimental value of U refers mostly to these atoms. The sensitivity to a and d sites, occupied by Fe and Ga, is much less (20 to 40%, depending on the reflection), and the sensitivity to h-sites, occupied by 0, is practically 0.[7]

The definition of strain used in this work is the fractional change in lattice parameter with respect to that of virgin GGG crystal. The strain may have a component $\epsilon^{\perp}$ in a direction perpendicular to the film surface and a lateral component $\epsilon^{\parallel}$. In general, both $\epsilon^{\perp}$ and $\epsilon^{\parallel}$ change the magnitude and the direction of a particular reciprocal lattice vector. These changes are related to the measurable change in the angular location of the Bragg peak.[7] X-ray diffraction alone gives no information on stress.

Detailed information about extended defects is much more difficult to extract from the rocking curve. If they occupy a sufficiently small volume, they are indistinguishable from point defects. If the extended defects involve gentle, long-range ($\sim 1\,\mu$m radius) distortion of the lattice, then they result in a broadening of the rocking curve. In this case, the mosaic-crystal theory[51] may be used to obtain estimates of their size, misorientation, and lateral variation in strain.[5,49]

The relationship between point defects, strain, extended defects, and dopant chemistry on one hand, and magnetic properties on the other, is poorly understood. We are not aware of any "first-principles" theoretical framework which would attempt to relate magnetism to the chemistry and geometry of implanted crystals. At low doses there is an approximately linear relationship between the shift in location of the FMR principal surface mode and dose, strain or stress. The proportionality constant roughly corresponds to the magnetostriction constant determined by external deformation of the virgin crystal. At higher doses the mode shift is no longer simply related to any of these. In some of the references a correlation is attempted in which the mode shift is equated to a change in H_k which is then related to the dose or maximum strain. This is erroneous for several reasons. The most important of these is that H_k saturates and decreases in regions of high damage so that the mode is localized and measures the change in H_k at a point far from the point of maximum strain. It is not clear whether the changes in other magnetic properties, such as M, A, H_1, γ, and α are due to strain or damage or chemistry, or a combination of all. Even worse, the magnitudes of these changes versus ion species, dose or depth are also poorly known. Ferromagnetic resonance spectra, when interpreted according to the model presented in Ref. 31, provide information about profiles of these magnetic properties.

IV. THE FITTING PROCEDURE

Crystalline profiles and magnetic profiles are obtained from the rocking curve and the FMR spectrum, respectively. Unfortunately, neither technique as presently used can directly yield the desired profiles from the respective measurement. Both techniques rely on choosing a trial distribution, calculating the corresponding spectrum, and comparing it to the experimental data. Since the spectra characteristic of various classes of profiles (unimodal versus polymodal, constant or increasing or decreasing with depth, etc.) have already been calculated, these serve as a guide in choosing the initial distributions. A trial and error procedure is then used until a satisfactory fit is obtained. A more sophisticated approach is the use of Jacobians to determine the changes in profile for a better fit. However, combination of this with least-squares fitting procedures has been singularly unsuccessful in converging to a satisfactory fit.

In the rocking curve, the angular range of nonzero reflecting power establishes the maximum strain, the most rapid oscillation establishes the total layer thickness, the area under the curve establishes the thickness-averaged structure factor; and the degree of smoothing is related to extended defects.[7] In the kinematical regime, the rocking curve and the strain and damage distributions are related through a Fourier transformation. However, the lack of phase detection precludes a direct inversion of the rocking curve.

In perpendicular FMR, the location of the highest mode yields an estimate of the maximum field for local uniform resonance H_{un}; the total number of surface modes yields an estimate of the ratio $A/(MT^2)$, where T is the layer thickness; the linewidth is linearly related to the damping parameter α; the relative amplitudes of the principal surface and body modes yield a value for surface to bulk magnetization ratio.[31,52] Some of this information is repeated in a different form for parallel FMR.

For both x-ray and FMR analyses the accuracy and uniqueness of a resulting distribution depend on several factors: the information content (i.e., structure) of the experimental data, the sensitivity of the experimental data to variations of the quantity in question, the extent to which other parameters produce similar effects and of course the accuracy or quality of the fit that is demanded. The interpretation of the rocking curve is less ambiguous than the FMR spectrum since the rocking curve depends very strongly on only one parameter, the strain distribution. The damage distribution though required for a fit at high doses and strain has a much smaller effect. As a consequence the strain profile can be quickly obtained with an apparent high accuracy, while the damage profile is less certain. Without a formal proof, it remains our opinion that the strain distribution corresponding to a given rocking curve is unique, except for mirror reflections. Typically the strain distribution is determined everywhere to a precision of a few percent of the maximum strain, and $\pm 2\%$ at the peak. The depth resolution is 50 to

200 Å depending on the particular distribution.

We describe the damage distribution by U the standard deviation of an assumed Gaussian distribution of random atomic displacements. The local structure factor has an exponential dependence $|F| \sim e^{-kU^2}$, and so the parameter U becomes a dominant factor in regions of high damage and has no effect in regions of low damage.[7] In a later section it will be shown that a linear relation between U and strain gives the best fit but that the proportionality constant varies with implant element. Thus the value of this constant is determined by the fitting process for medium to high doses.

For the samples studied here, the number of surface modes excited by perpendicular FMR ranges from 1 to 11. If their locations and amplitudes are used as inputs, there are from 2 to 22 data points. The major parameters which determine mode locations and amplitudes are the field for uniform resonance H_{un} and the ratio A/M. When several modes are present, the FMR spectrum appears to be uniquely related to the distribution of H_{un} provided this distribution is unimodal. In such cases the precision of the determination is within a few percent of the maximum everywhere, and $\pm$ 3% at the peak. For unimodal distributions, the depth-averaged A/M is also determined to $\pm$ 10%, but the sensitivity to the shape of this distribution is relatively poor. The same remarks apply to the distribution of M. Parallel FMR is used to separate the various components of H_{un}. However the resolution of parallel FMR is less than half that of perpendicular FMR, and the overlap of modes vitiates accurate amplitude measurement.[31]

If the magnetic profiles are polymodal, we are unable to determine a unique profile from a single set of spectra. One must then resort to etching (or preferably ion-milling, since it removes the material more uniformly) and reconstruct the profiles as described in Ref. 31. The etch or milling steps must be small (100–200 Å) since larger etch steps leave room for multiple interpretations of the spectra. The above discussion suggests the fitting procedure we followed.

For all samples the strain and damage profiles were first obtained. Magnetic profiles were estimated by assuming a unique relationship to exist between ΔH_{un} and $\Delta\epsilon^{\perp}$ for each implanted species. For neon and helium, this relationship was immediately shown to be linear at low doses with a clear saturation of ΔH_{un} for what we term medium doses. In this range the saturation can be represented empirically or by some convenient mathematical form. We found it convenient and satisfactory to assume a form

$$\Delta H_{un} = K\,[\Delta\epsilon^{\perp} - b\,(\Delta\epsilon^{\perp})^3] \qquad (1)$$

The magnitudes of the linear and cubic terms were adjusted to give a best fit to the spectra for all low to medium doses.

The assumption that ΔH_{un} and $\Delta\epsilon^{\perp}$ are uniquely related was not arbitrarily made. In previous publications, the authors have separately studied the same low-dose He-implanted garnet with properties similar to those of some of the present samples. The magnetic profiles were determined by one of the authors[31] independently of any x-ray results, and the crystalline profiles were obtained by the other author[7] without FMR inputs. Upon comparison, the ΔH_{un} and $\Delta\epsilon^{\perp}$ profiles agreed with each other to $\pm$ 2% of the peak values.

Various features of the FMR spectra imply differences in surface and bulk values of other magnetic parameters. Differences in the linewidth require a change in α; relative mode amplitudes may dictate a change in M; comparison of $\perp$ and $\parallel$ modes may require a change in H_1 or γ; FMR as a function of polar angle about $\langle 1\bar{1}0\rangle$ axes places limits on the allowed changes in H_1. However there is relatively poor sensitivity to the actual profile shape of these magnetic properties. A convenient assumption that is consistent with experimental data is that these changes are also linearly related to $\Delta\epsilon^{\perp}$. The peak value for each distribution is then independently adjusted to fit the appropriate spectrum.

In the case of low to medium doses of neon and helium, this approach produced excellent fits to the FMR spectra. For all arbitrary deviations from this relationship that were tested, the quality of fit rapidly deteriorated. At very high doses the structure of the FMR spectra changed so radically, that we were unable to use the strain data to obtain magnetic profiles. In this dose range the bimodal profile of H_{un} was determined independently of strain, and with reduced precision by etching and using the methods of Ref. 31.

For the samples implanted with hydrogen, the assumption of a unique relationship between ΔH_{un} and $\Delta\epsilon^{\perp}$ was immediately shown to be false. Nevertheless, since the magnetic profiles are unimodal, they could be obtained directly from the FMR spectra, without the need to resort to etching.

V. RESULTS AND DISCUSSION

A. Experimental and calculated spectra

Since neither rocking curves nor FMR spectra corresponding to a wide range of doses of ion-implanted garnets have been published, we include here some of our experimental data. In addition to showing their structural peculiarities, the figures include calculated spectra showing the quality of fit that is obtainable. For this quality of fit the distributions of $\Delta\epsilon^{\perp}$ and ΔH_{un} have the accuracy quoted earlier except for high doses where portions of the film become amorphous or paramagnetic.

Figures 1(a), 1(b), and 1(c), respectively, show the experimental (dashed) and calculated (solid) rocking curves for several doses of Ne^+, He^+, and H_2^+ implanted garnet. All three sets have several features in common: the single sharp peak near the origin corresponding to diffraction by the deep, unimplanted, bulk portion of the film; the oscillatory structure which extends to lower angles and becomes less intense with increasing dose; and the envelope shape characteristic of unimodal distributions. For all cases shown, the calculated plane-wave solution was convolved with the incident beam, whose angular divergence distribution is approximated by a Gaussian with a standard deviation of 8 arcsec.

Figures 2(a), 2(b), and 2(c), respectively, show the perpendicular FMR spectra for the same samples. The spectra are presented in stick-diagram form, the solid and open rectangles corresponding to measured and calculated modes, respectively. For clarity, the modes (experimental and calculated) are shown adjacent to each other, without overlap. The actual field is located at their boundary. The discrepan-

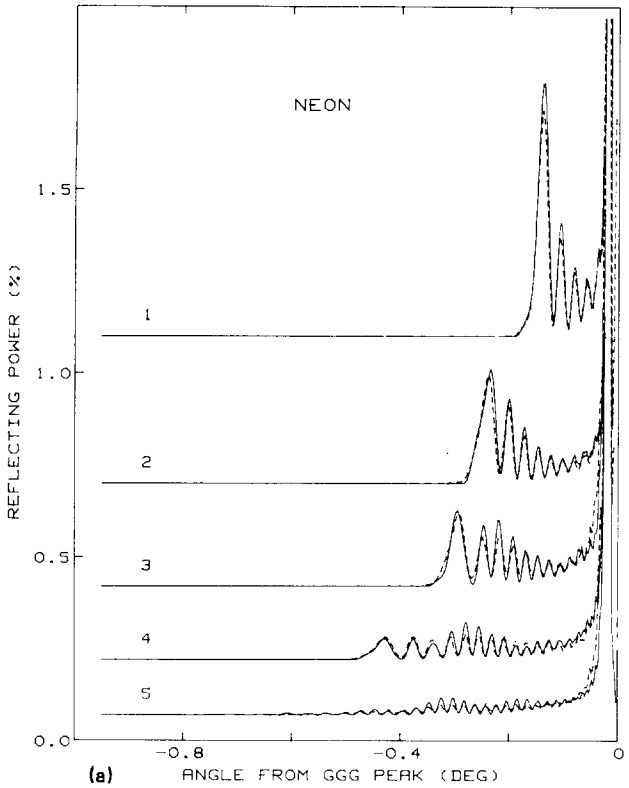

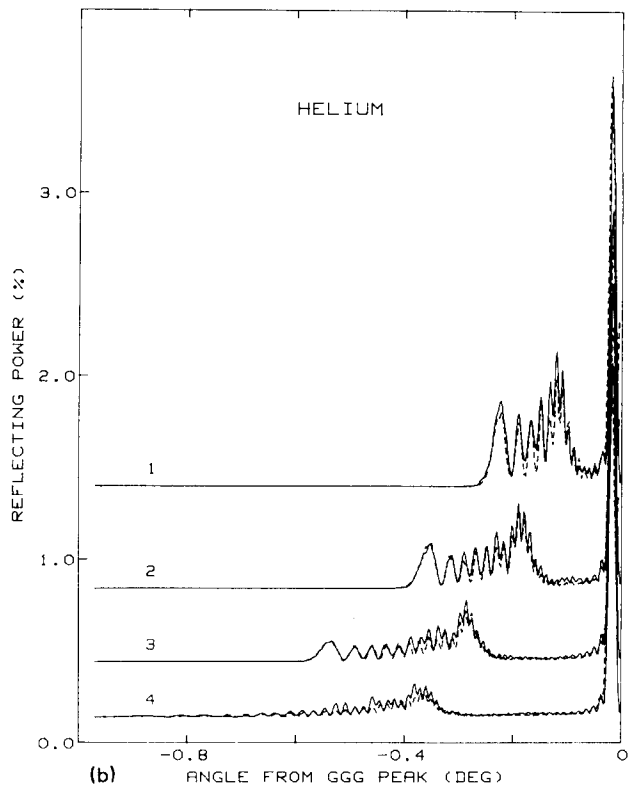

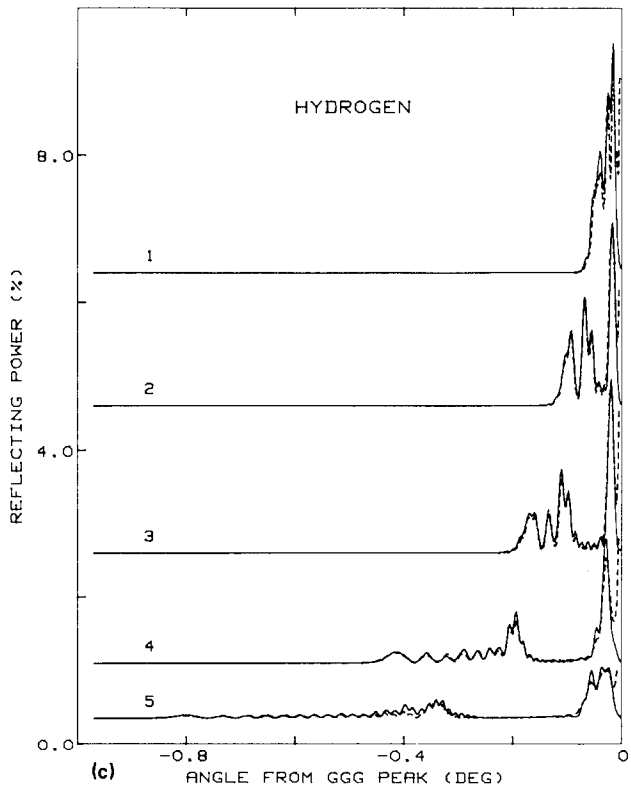

FIG. 1. (a) Measured (dashed line) and calculated (solid line) Cu K_α (444) rocking curves for 190 keV Ne^+ implantation. Doses are 0.5, 1.0, 2.0, 3.0, and $5.0\times10^{14}/cm^2$ for curves 1–5, respectively. (b) Cu K_α (444) rocking curves for 140 keV He^+ implantation. Doses are 3.0, 6.0, 12, and $20\times10^{15}/cm^2$ for curves 1–4, respectively. (c) Cu K_α (444) rocking curves for 120 keV H_2^+ implantation. Doses are 2.0, 3.0, 5.0, 20, and $40\times10^{15}/cm^2$ for curves 1–5, respectively.

cy between calculated and measured mode location is as a rule less than $\pm$ 10 Oe, rarely becoming as large as 50 Oe for some of the high dose cases. Mode amplitudes are indicated by the relative height of the rectangles. Experimental modes with amplitudes less than 10% of the principal (or first) surface mode, and nearly 0 amplitude theoretical modes where no experimental mode is seen, are also indicated by vertical arrows. The 50 Oe width of the rectangles does not reflect the actual mode linewidth, which increases with dose from 70 Oe (bulk modes) up to ~150 Oe (surface modes for highest doses).

Only spectra for the three lowest doses of hydrogen im-

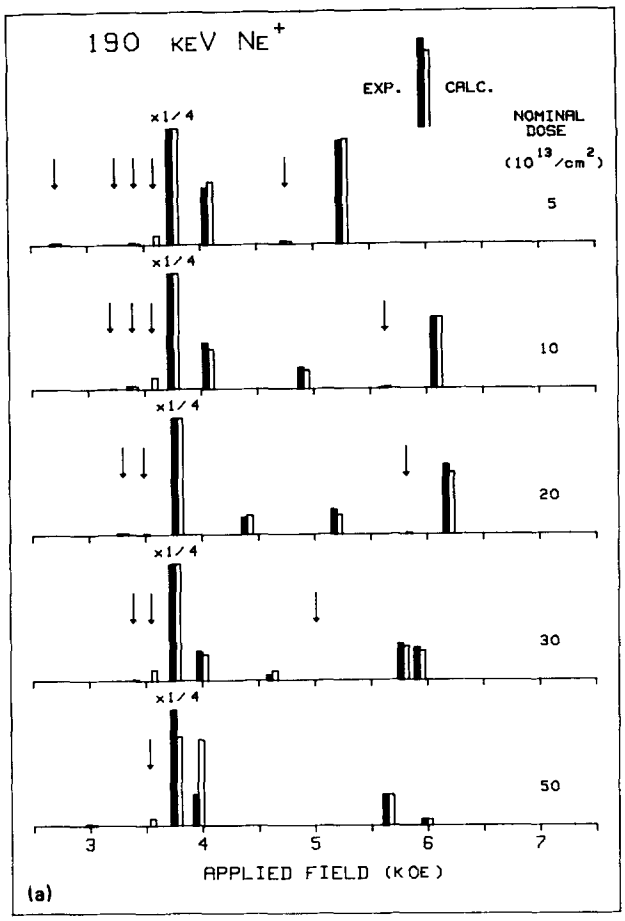

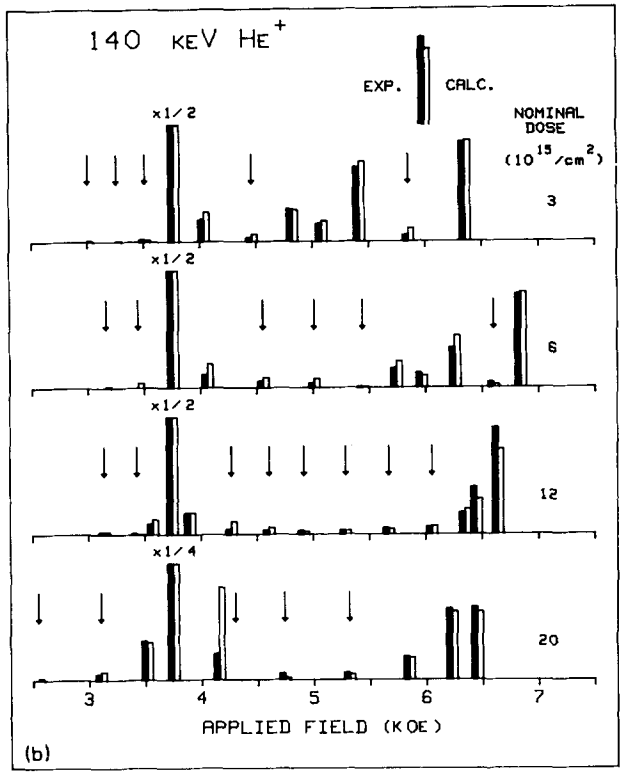

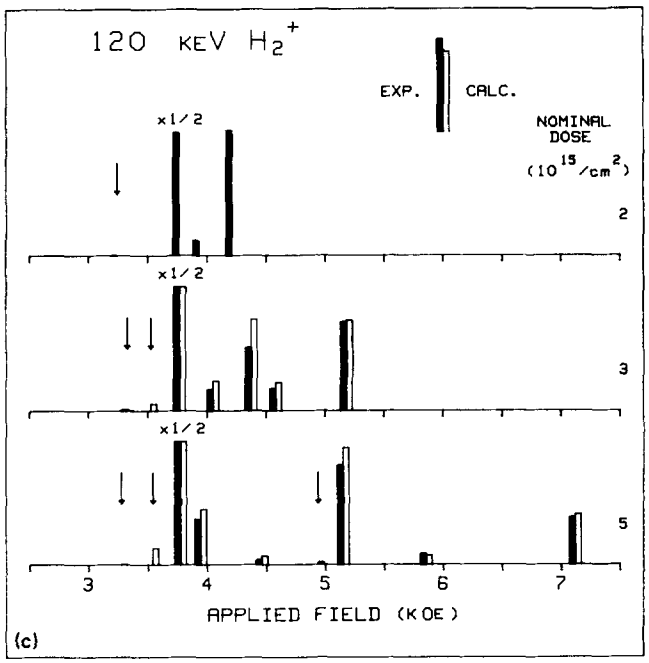

FIG. 2(a) Measured (solid rectangles) and calculated (open rectangles) ⊥ FMR spectra for the Ne^+ samples of Fig. 1(a). (b) ⊥ FMR spectra for the He^+ samples of Fig. 1(b). (c) ⊥ FMR spectra of the three lower dose H_2^+ samples of Fig. 1(c).

plantation are shown in Fig. 2(c). The higher-dose spectra were excluded because of unusual lineshapes of the lower surface modes. A plausible explanation for these shapes is that with large anisotropy the static magnetization is not completely aligned for applied fields corresponding to the lower modes. Although surface modes would still exist in this situation, they could not be calculated by the methods used in this study.

The depth-dependence of the rf magnetization in FMR provides a convenient classification of modes. In the present

figures, the largest mode, occurring at ~3750 Oe, is the main bulk mode, while modes at lower fields are predominantly sinusoidal bulk spinwave modes. The modes found at fields above the main mode are largely confined to the implanted layer and are called surface modes.[31] For low doses, the amplitudes of the surface modes generally follow an alternating large–small sequence which is characteristic of certain unimodal distributions of H_{un}.[52] This is seen for the lowest three neon doses, the lowest two helium doses and all three hydrogen doses.

An important feature is observed on comparing the spectra for the lowest and highest doses in the neon and helium series. Although the nominal doses vary by an order of magnitude, the separation between the principal surface and bulk modes changes by less than 30% in both cases. However the high dose spectra have a drastically different character. In these cases the magnetic profiles become bimodal. The details of the bimodal profiles could only be elucidated by analysis after progressive etching.

The bimodal character was first established for the third helium implant with dose $1.2\times10^{16}/\text{cm}^2$. This case showed at least 10 surface modes in a complex spectrum unlike anything seen in earlier work. The development of this spectrum with etching was even more bizarre as seen in Fig. 3(a). Mode locations are indicated by circular symbols (or elliptical symbols for less certain locations); mode amplitudes are given at selected depths. Question marks indicate amplitudes uncertain by more than a factor of two. Also shown are the cumulative etch-time intervals, and vertical arrows which indicate depths obtained by analysis of x-ray rocking curves. The unetched spectrum is identical to one of the spectra in Fig. 2(b). The evolution of this spectrum with etch depth is quantitatively and qualitatively different from that of a lower dose, but identical energy, He^+ implantation in a similar garnet (see Fig. 5 of Ref. 31 for a comparison).

Figure 3(b) shows the calculated spectrum for the etched sample. To obtain this structure it was necessary to use a bimodal profile for H_{un} with extreme variations in magnetic profiles to be discussed below. Although there are small discrepancies of detail between Figs. 3(a) and 3(b), the sensitivity of the calculated spectrum to the extreme variations in magnetic profiles is so large that we accept this result as sufficiently accurate.

In addition to this case, the etching and fitting procedure was repeated for the neon implantation with dose $3\times10^{14}/\text{cm}^2$. A similar profile was required and the quality of fit is similar to that shown in Figs. 3(a) and 3(b).

B. Profiles of perpendicular strain

The strain profiles obtained from the rocking curves of Fig. 1 are shown in Figs. 4(a), 4(b), and 4(c) for Ne^+, He^+, and H_2^+ implantations, respectively. In each figure the distributions are labeled to show correspondence with the appropriate rocking curves. Since the (444) reflection used is symmetric about the film normal, only the perpendicular strain is measured. The unimplanted region shows an as-grown component of strain. Assuming that for any single wafer this strain is constant and independent of location on

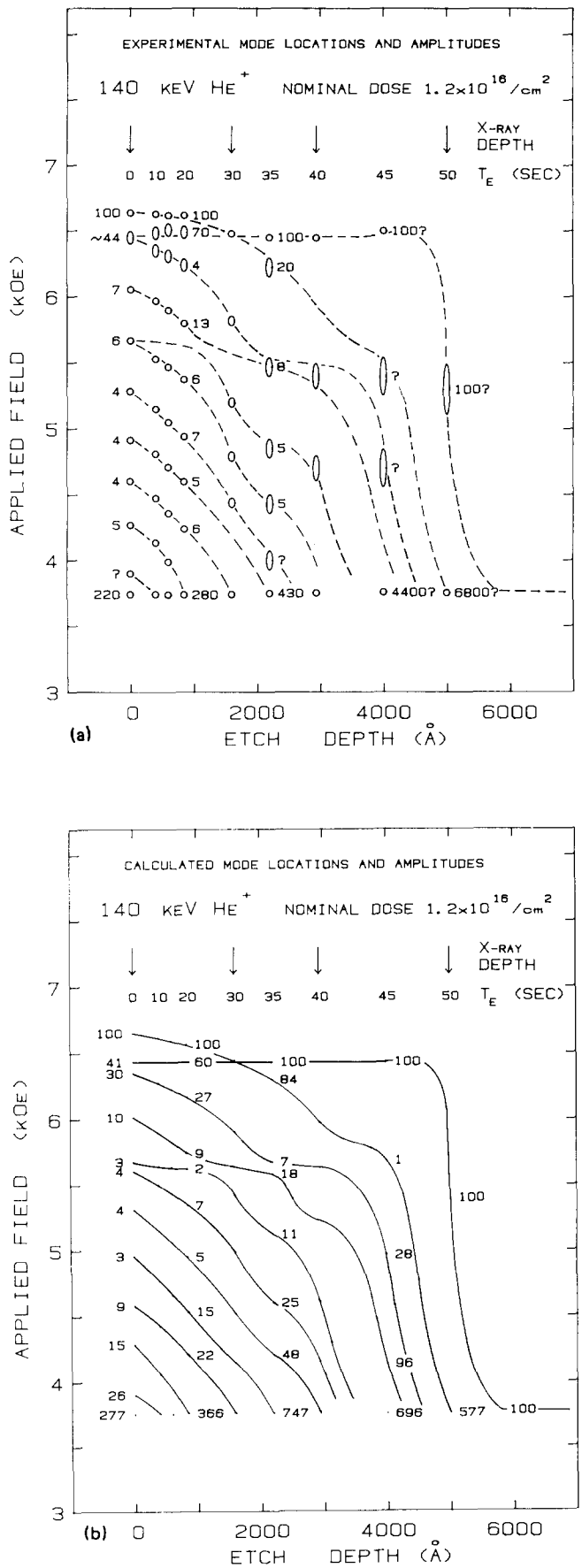

FIG. 3(a) Experimental ⊥ FMR spectrum vs etch depth for the sample implanted with 140 keV He^+, $1.2\times10^{16}/\text{cm}^2$. (b) Calculated ⊥ FMR spectrum corresponding to Fig. 3(a).

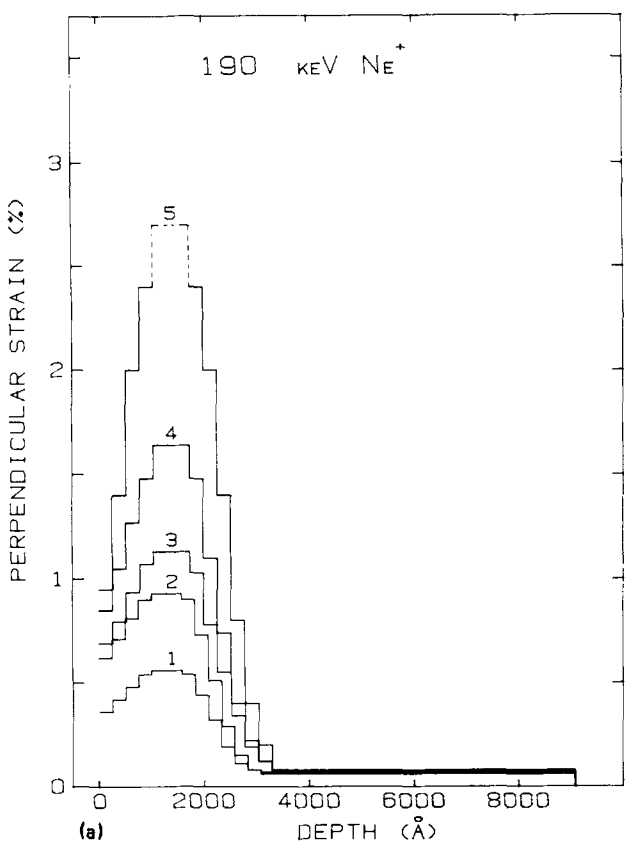

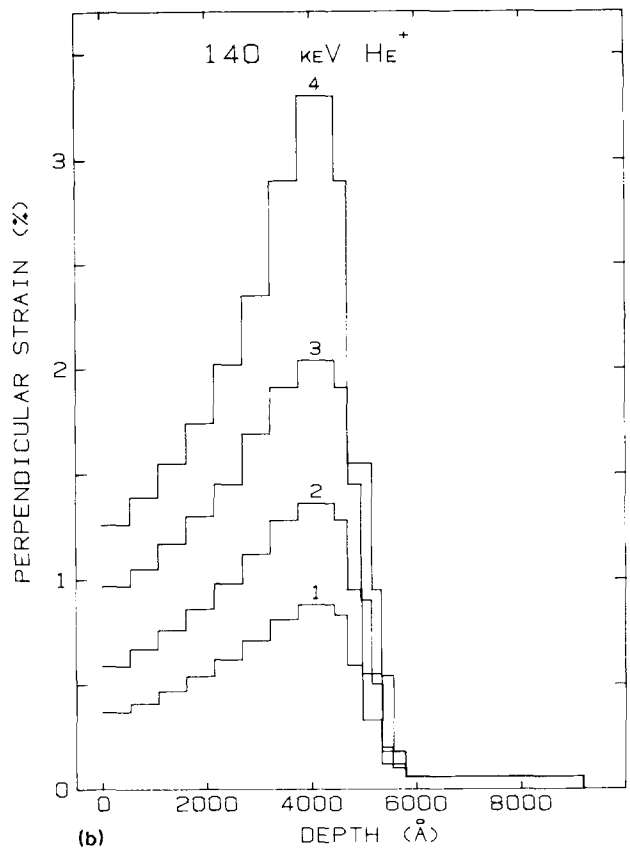

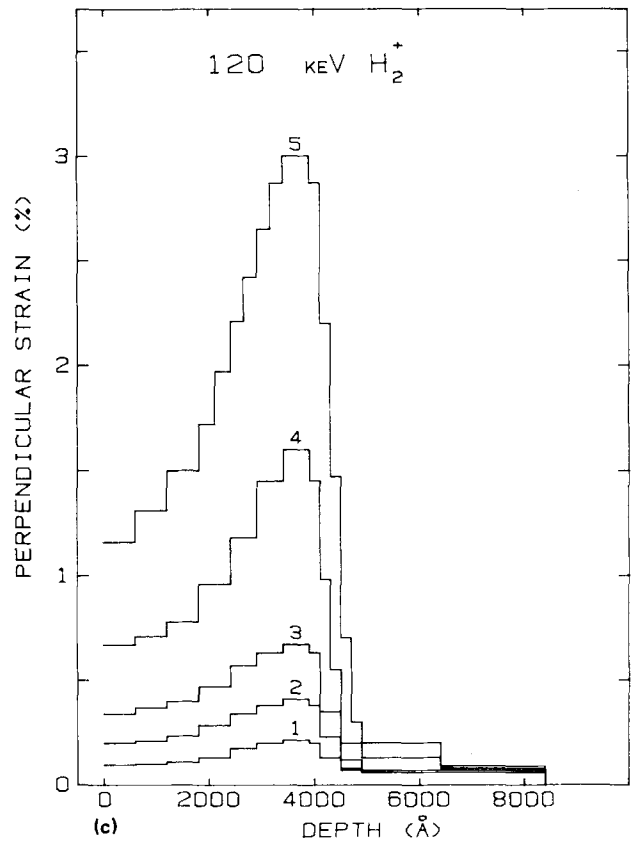

FIG. 4(a) Perpendicular strain profiles of Ne^+ implanted samples. The distributions are labeled to show correspondence with the rocking curves of Fig. 1(a), from which they were obtained. (b) Perpendicular strain profiles of He^+ implanted samples. (c) Perpendicular strain profiles of H_2^+ implanted samples.

the wafer, the small spread observed in the measured value verifies the reproducibility of experimental rocking curves stated earlier. The implanted regions shown on the left in these figures have thicknesses which depend on implanted species and energy. For computational convenience the distributions are represented in laminar form, the number of laminae being approximately the minimum required for a good fit.[7] This number increases with increasing strain, as

seen in the figures. In the case of neon implantation the damage becomes so large that there is no measurable diffraction from regions where the strain exceeds 2.5%. The maximum strain for the highest dose in Fig. 4(a) cannot be determined by this method and the peak of the profile shown by dotted lines is simply an extrapolation.

For each species the general features of the profiles conform to expectations based on LSS theory. Going from Ne^+ to He^+ to H_2^+ the distributions become sharper and increasingly asymmetric about the maximum strain. The magnitude of the maximum strain below amorphousness is about 2.5% for Ne^+, and by a slight extrapolation 3.4% for He^+ and 3.9% for H_2^+. For each species the surface strain is less than half of the maximum strain. The thicknesses of the strained layer are 3300, 5800, and 4900 Å, respectively. The total thickness, including the bulk region, is 9200 Å for the Ne^+ and He^+ implanted wafer, and 8400 Å for the H_2^+ implanted wafer. Both values are in reasonable agreement with the approximate values determined optically by the supplier.

For the two highest doses of H_2^+ implantation [Fig. 4(c), distributions 4 and 5], our resolution is sufficient to show that the presumed bulk region is not really uniform. A two-layer representation of the strain profile in the bulk is shown since the resolution does not permit greater detail. The variation shown is required to fit the low-angle features of the rocking curve. The difference in strain between the two layers increases in proportion to the maximum strain. This behavior as well as the thickness and location of the region of higher strain leads us to conclude that the increased strain is due to the presence of implanted hydrogen. For 120 keV H_2^+, according to theory most of the stopped hydrogen atoms are located in a region about 2000 Å wide at a distance of 4500 Å from the surface.[53] The region of increased strain in the bulk region is consistent with this calculation. For these doses, the relative atomic concentration of hydrogen is 2% to 4%, and the presumed dopant-induced strain is 4% of the maximum strain induced by damage. This relation may hold for other implanted species but cannot be determined by the rocking curve method. For other dopants the implanted layer is rendered amorphous for doses corresponding to dopant concentrations well below 1%.

For each implanted species there are two curious features involving the relation between maximum strain and dose, and the ratio of surface strain to maximum strain. First, the maximum implantation-induced strain $\Delta\epsilon_{max}^{\perp}$ does not behave smoothly as a function of nominal dose. For example, the values of $\Delta\epsilon_{max}^{\perp}$ in Fig. 4(a) are in the ratios 1:1.8:2.1:3.2:5.4. The normalized nominal doses form a different sequence 1, 2, 4, 6, and 10. For hydrogen [Fig. 4(c)], the values of $\Delta\epsilon_{max}^{\perp}$ are in the ratios 1:2.3:3.9:9.8:18.8 while the normalized nominal dose sequence is 1, 1.5, 2.5, 10, and 20. Data for helium are also inconsistent but in a third way. If the nominal doses are taken at face value, there is no discernible unique relationship between maximum strain and dose. Since implantation was done in another laboratory, we are unable to assess the accuracy of the doses. The second feature is that the detailed shape of the strain distribution (in particular the ratio of surface strain to peak strain) does not show a systematic trend with increasing dose. Fortunately the existence of pairs of nominally identical samples for each species and dose has enabled a partial resolution of this puzzle. The rocking curves obtained from each pair of samples are in most cases decidedly different giving rise to an inconsistency in the ratio of surface to peak strain. While the maximum strain values for each pair do not differ by more than 15%, a discrepancy develops between this region and the surface, becoming as large as 250% at the surface. It was gratifying that this same inconsistency was found in the FMR spectra and their corresponding H_{un} profiles. The lack of systematic trend mentioned above is simply a continuation of this inconsistency. The actual reason for these variations in strain and magnetic profiles for nominally identical samples remains unknown. This inability to manufacture reproducible samples has hampered our attempt to determine the dose dependence of strain and magnetic profiles. Serious inconsistencies in the properties of implanted garnets versus dose have been reported by at least two other laboratories.[54,55]

C. Lateral strain and stress

An important characteristic of ion-implanted single crystal layers is the compressive stress in the implanted region. Its existence implies that at least up to a certain dose, implantation causes a tendency toward an isotropic or nearly isotropic expansion of the unit cell. But at least initially the registry with undamaged crystal contrains the implanted layer to expand only in a direction perpendicular to the surface.[7] Therefore the implanted layer and the much thicker substrate are in lateral compression and lateral tension, respectively. The depth-averaged compressive stress has been measured by a beam cantilever method.[14] For 100 keV Ne^+ implantation with increasing doses ranging from 10^{13} to $10^{15}/cm^2$, in Ref. 14 the average stress initially increases linearly with dose, then saturates, and finally decreases to the limit of detection. Over this range we find that the perpendicular strain continues to increase with dose up to amorphousness. Three possible reasons for the decrease of stress come to mind: (1) with increasing dose the modulus of elasticity E of the implanted layer diminishes by more than an order of magnitude; (2) dislocations are formed to accommodate the lattice mismatch and allow the unit cell to relax back to a cubic shape; and (3) a phase transition occurs such that the new equilibrium shape of the unit cell is rhombohedral.

By measuring lateral strain we have attempted to determine the role played by the second possibility in the mechanism of stress relaxation. For the Cu K_α (880) $\gamma_0 > |\gamma_H|$ reflection in ⟨111⟩ garnet the glancing angles of incidence and diffraction are 80° and 9.5°, respectively. In the $\gamma_0 < |\gamma_H|$ reflection the directions of incidence and diffraction are reversed. For both cases the rocking curve measures lateral in addition to perpendicular strain. In the $\gamma_0 < |\gamma_H|$ reflection the sensitivity to lateral strain is even greater than to perpendicular strain. In a helium implanted sample with a maximum perpendicular strain of 0.82%, previous measurement showed[7] that lateral strain was below the limit of detection ($\sim$0.03%).

In the present study we selected the neon distribution no. 4 ($\Delta\epsilon^{\perp}_{max} = 1.57\%$) and the helium distribution no. 3 ($\Delta\epsilon^{\perp}_{max} = 2.00\%$) because the strain is high but the damage is below the level of amorphousness (see the next section for results on damage). The nominal dose for neon case no. 4 is greater than the dose for which the stress rapidly diminishes, as reported in Ref. 14. Our present result is that for both Ne^+ and He^+ distributions the measured lateral strain at any depth is not greater than 0.03%. Thus, even though the stress may have relaxed, the implanted unit cell has not returned to cubic shape. This rules out possibility no. 2 as the mechanism of stress relaxation. We have no direct evidence for a large reduction in E. Crystalline and amorphous alloys and glasses of the same composition usually have similar elastic properties, but this may not hold for structures like garnet where bonding by oxygen is an essential part of the structure. An alternative hypothesis is that the equilibrium shape of the unit cell in the implanted garnet layer becomes, at a certain dose, rhombohedral. A possible mechanism for this transition has been suggested by W. L. Johnson.[56] Due to the interaction of the local stress field of a Frenkel pair with the macroscopic (average) stress, the energy of the Frenkel pair is not invariant under rotation. During implantation at a certain dose this energy is minimized by an uniaxial orientation of Frenkel pairs which reduces the macroscopic stress. When this occurs the perpendicular strain no longer has a Poisson contribution. For this and higher doses $\Delta\epsilon^{\perp}$ should show a different behavior from that at lower doses. We are unable to verify this since the actual doses are uncertain and for nominally identical implantation the strain distribution is not reproducible.

The assumption that in implanted ⟨111⟩ garnet the equilibrium unit cell becomes rhombohedral is supported by a measurement of the stress distribution[16] in a magnetic garnet implanted with 200 keV Ne^+ at a dose of $2\times10^{14}/cm^2$. According to this reference, in the implanted layer the stress distribution is bimodal. The 1000-Å-thick regions near the surface and near the interface with unimplanted material are under substantial and comparable lateral stress. In the intermediate region, also 1000 Å thick, where the perpendicular strain and the damage are greatest, the stress is barely measurable. The existence of compressive stress in the outer region is unexplained if relaxation occurs by a crystallographic decoupling of highly implanted from less implanted region. But if the relaxation is accomplished by a local transition to an equilibrium rhombohedral unit cell, then at a given depth the stress depends on the degree of this transition. In this case two regions with the same sign of the stress may be separated by a region with zero stress. Since even at high doses we have measured the lateral strain to be zero, henceforth we shall drop the term "perpendicular" when we speak of strain.

D. Damage profiles

For the present range of doses, for each species the area under the rocking curve changes by roughly one order of magnitude. Since the layer thickness does not decrease with increasing dose, the only possible interpretation is that the magnitude of the structure factor F decreases. Amorphousness corresponds to $|F|\sim0$. Small strains (0.1 to 0.5%) are easily measured with good accuracy. In this region the structure factor is essentially unchanged and no information can be obtained about the damage profile. When the maximum strain reaches about 2.5% for neon, 3.4% for helium or 3.9% for hydrogen, the structure factor in the region of maximum strain has decreased to nearly zero and above this strain no measurable diffraction occurs. As the peak strain falls below this critical value, the local structure factor rises sharply, the best fit being a negative exponential in $(\Delta\epsilon)$.[2] Since the structure factor is known to depend in this same way on U (the standard deviation of the assumed Gaussian random atomic displacements) it follows that the peak value of U is linear in $\Delta\epsilon$. Elsewhere in the profile, the sensitivity is such that U cannot be determined with equal precision and we can only state that when the strain is high enough to give a determination of U, the peak value occurs in the region of maximum strain. Since it varies linearly in this region, it is a reasonable hypothesis that this relation holds at all depths and strains, in agreement with Ref. 7. This is consistent with the idea that the damage is the source of the strain.

With this assumption, excellent fits have been obtained for all doses. The proportionality constant between U and $\Delta\epsilon$ has the value 0.25, 0.18, and 0.13 Å/% for Ne^+, He^+ and H_2^+ implantation, respectively. The different effective levels of damage for the same strain are due to the discriminating sensitivity of the (444), (888), and (880) reflections to the c

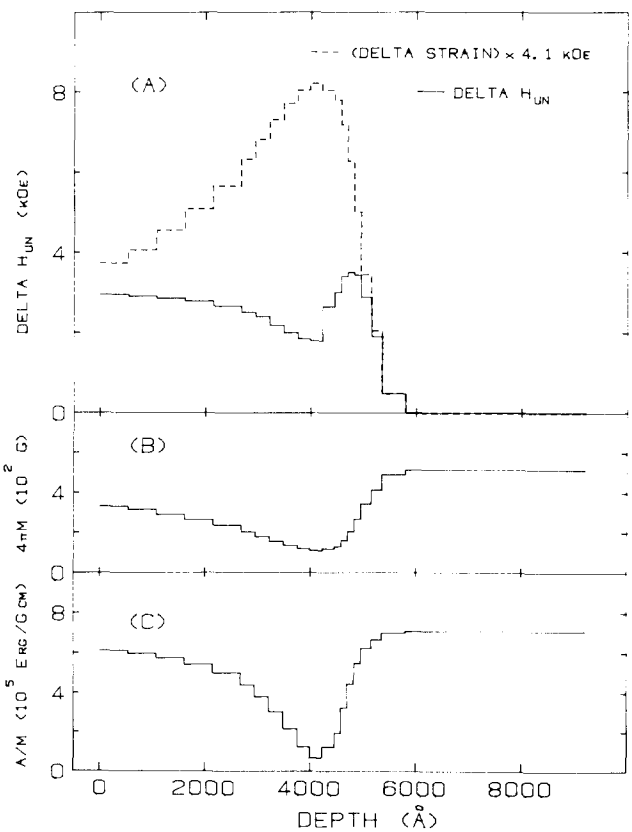

FIG. 5. Profiles corresponding to Fig. 3: (a) ΔH_{un} (solid) and $\Delta\epsilon$ (dashed); (b) magnetization $4\pi M$; (c) ratio A/M.

sites occupied by the heavy elements Y, Gd, and Tm. The implication is that for the same strain, neon ions damage the c-sublattice more severely than helium or hydrogen ions. This is in agreement with the ballistics of implantation in polyatomic materials.[48]

At high doses the broadening of (880) reflections indicates the presence of lateral nonuniformities attributable to extended defects. The resolution is not sufficient to provide quantitative information about their density or structure. As we have shown, these defects do not result in any measurable lateral strain.

E. Magnetic properties versus strain for He^+ and Ne^+ implantation

The local field for uniform resonance H_{un} in ⊥ FMR is

$$H_{un} = \frac{\omega}{\gamma} - H_k + 4\pi M + \frac{2}{3} H_1, \tag{2}$$

where ω is the microwave angular frequency, γ is the gyromagnetic ratio, H_k is the uniaxial anisotropy field, $4\pi M$ is the saturation magnetization, and H_1 is the cubic anisotropy field. The change in H_{un} is specified by ΔH_{un}, the difference between its value and that in the bulk region. Of all magnetic properties obtainable by FMR, the distribution of ΔH_{un} is determined with the highest precision. However for high doses, substantial changes in other parameters are demanded by the resonance spectrum. Even though these changes are not known with the same precision, their general features are incontestable. A good example is shown in Fig. 5 for the helium implantation with dose $1.2 \times 10^{16}/cm^2$. This dose is not sufficient to give a nonmagnetic layer but produces extreme variations in almost all magnetic parameters and gives a very rich spectrum in ⊥ FMR with eleven surface modes as shown in Figs. 2(b) and 3(b). Figure 5(a) shows the profile of ΔH_{un} (solid line) and the strain profile multiplied by 4.1 kOe/% (dashed line). This choice of multiplicative constant is made clear below. Although the strain profile is unimodal, the distribution of ΔH_{un} is bimodal and no longer resembles

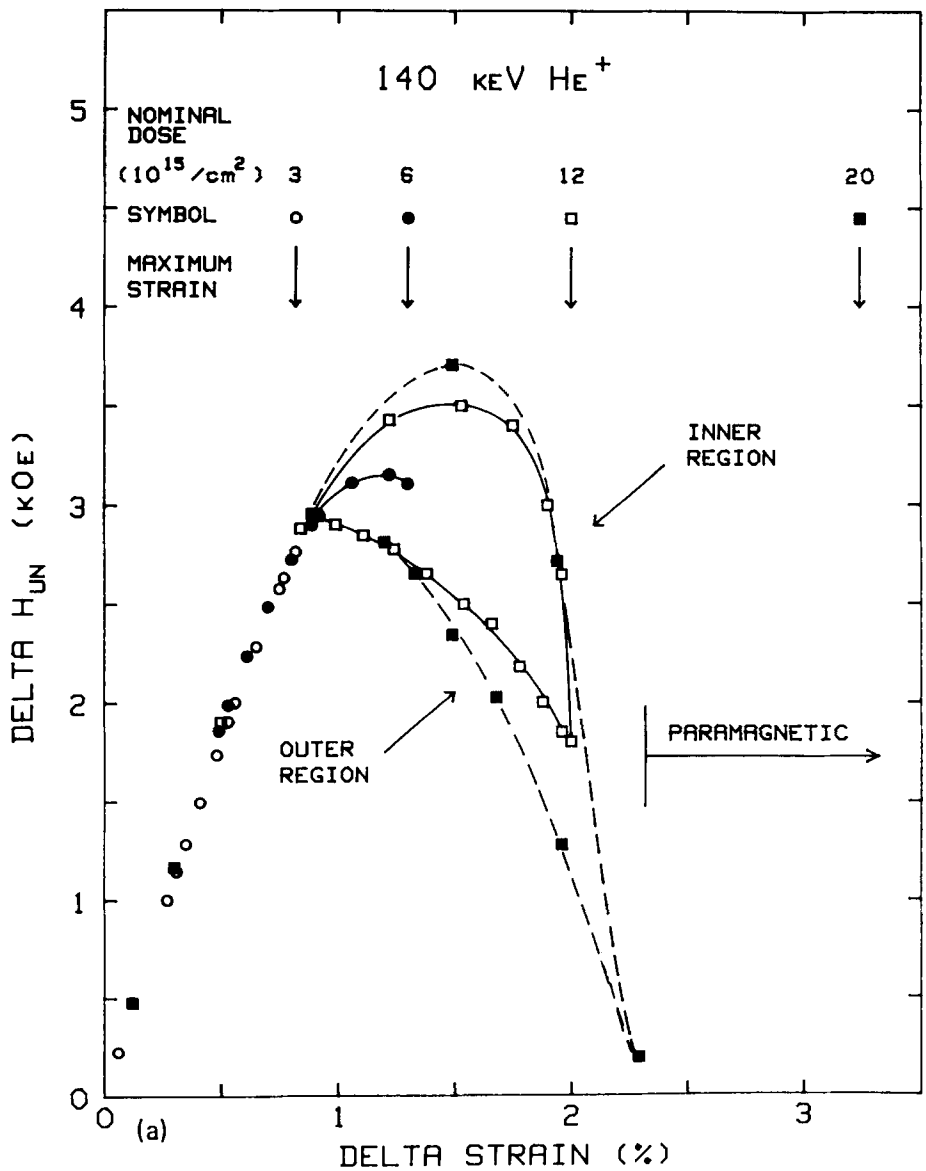

FIG. 6(a). ΔH_{un} vs $\Delta\epsilon$ for four He^+ doses. Each set of points corresponding to one dose is represented by its own symbol. Nominal doses and $\Delta\epsilon_{max}$ values are also indicated.

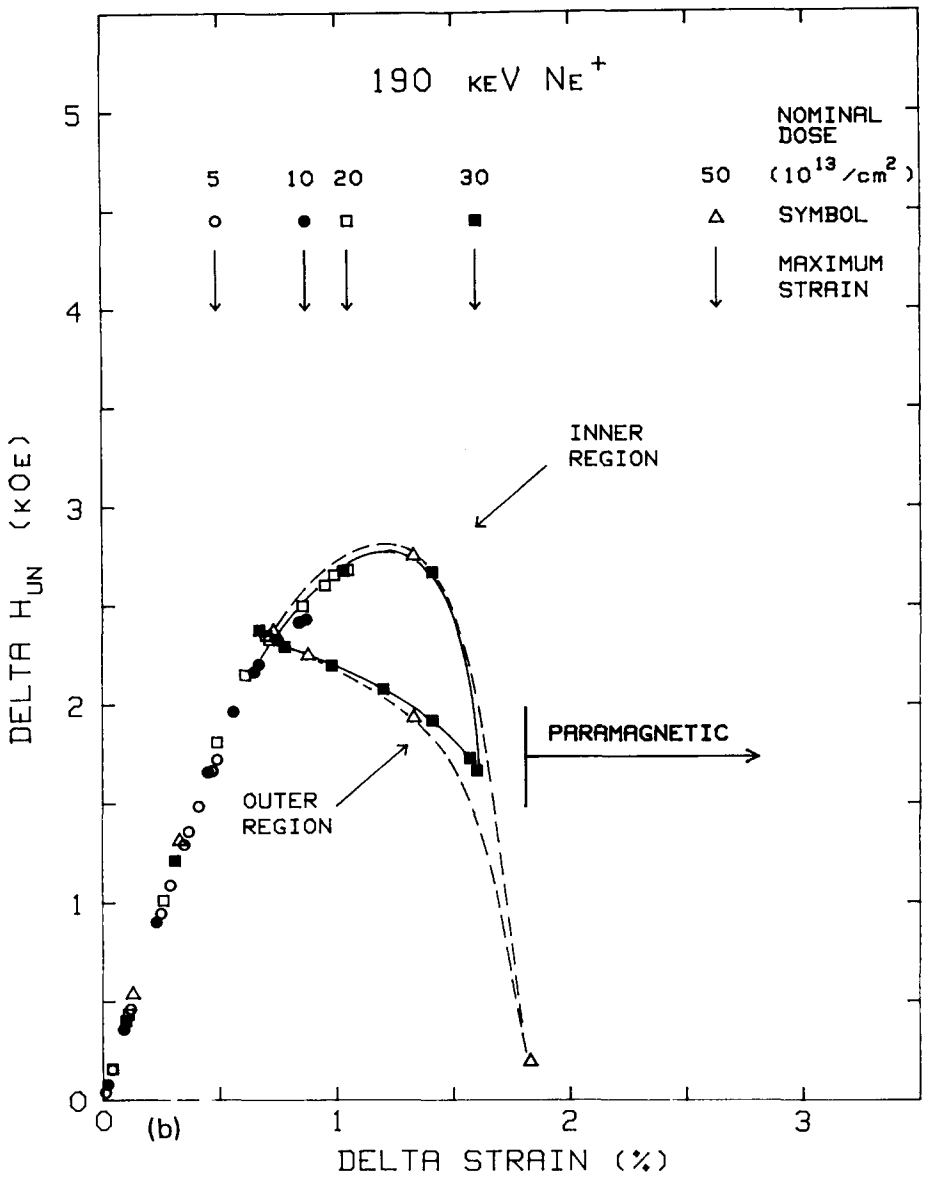

FIG. 6(b) ΔH_{un} vs $\Delta\epsilon$ for five Ne^+ doses.

the strain profile. The profiles of $4\pi M$ and A/M are shown in Figs. 5(b) and 5(c). At the location of maximum strain there is an 80% reduction in $4\pi M$ and a 98% reduction in exchange constant, A. These extreme variations are required to produce the FMR spectra of Fig. 3(b).

The relationship between ΔH_{un} and $\Delta\epsilon$ may be obtained by considering their respective values for all doses and depths. Figure 6(a) shows the values of ΔH_{un} versus $\Delta\epsilon$ obtained for all doses of helium implantation. A different symbol is used to represent each set of points corresponding to a particular dose. The nominal doses and the values of $\Delta\epsilon_{max}$ are also shown. If we limit attention to the two lower doses for which $\Delta\epsilon_{max} < 1.3\%$, all points lie on a single curve. In this dose range the relationship between ΔH_{un} and $\Delta\epsilon$ is unique and independent of dose or depth. As mentioned in a previous section, for pairs of samples with nominally the same implantation, the values of $\Delta\epsilon_{max}$ are nearly the same, but strain values towards the surface differ by a factor as large as 2.5. Even with such differences in profile the relationship shown in Fig 6(a) is valid.

The initial slope of the curve is 4.1 kOe/%. As we shall show, in the linear region approximately 98% of ΔH_{un} is due to the change in uniaxial anisotropy H_k. If the change in H_k is attributed to magnetostriction using bulk values of Young's modulus ($E = 2.0\times10^{12}$ dyn/cm^2), Poisson's ratio ($\nu = 0.29$) and magnetization ($4\pi M = 510$ G), one obtains a value of -3.6×10^{-6} for the magnetostriction constant λ_{111}. This number is higher than but in reasonable agreement with the value -3.4×10^{-6} estimated from the nominal composition and the tables given in Ref. 39. Thus we conclude that, at least for He^+, at low doses the principal source of ΔH_k is $\Delta\epsilon$ and that the relationship is the same as for external elastic deformation (magnetostriction).

For $\Delta\epsilon_{max} \gtrsim 1.3\%$ the dependence of ΔH_{un} on $\Delta\epsilon$ is much more complicated. First, ΔH_{un} saturates at a value 3.6 kOe at strain $\Delta\epsilon = 1.5\%$ and then decreases to a value near 0 at $\Delta\epsilon \approx 2.3\%$ where the material becomes paramagnetic. The material remains nonferrimagnetic up to the highest observed strain $\Delta\epsilon = 3.30\%$ where the material is nearly amorphous. Second, in the region where ΔH_{un} is saturating and

decreasing with strain, the relationship is no longer unique. The solid and dashed lines, respectively, connect the points obtained for two different doses where $\Delta\epsilon_{max}$ is equal to 2.00% and 3.30%. In each case there are two relations between ΔH_{un} and $\Delta\epsilon$. If the implanted layer is subdivided into two regions, one (the outer) includes all points from the surface up to the location of the peak strain, and the other (inner) region includes points from the peak strain down to the interface with unimplanted material. These regions have a different relation between ΔH_{un} and $\Delta\epsilon$. Another intriguing feature is the lower saturation for $\Delta\epsilon_{max} < 1.5\%$ compared to the peak value for higher strains. For now we defer discussion of the possible reasons for this behavior.

A plot of ΔH_{un} vs $\Delta\epsilon$ for all neon doses is shown in Fig. 6(b). The general features seen with neon are the same as with helium. The initial slope of the curve is 4.1 kOe/%, again supporting the conclusion that at low doses the phenomenon giving rise to ΔH_k is magnetostriction. The important differences between Ne^+ and He^+ implantation are the lower peak value of ΔH_{un} (2.8 kOe vs 3.6 kOe) and the lower strain (1.8% vs 2.3%) for which the material becomes paramagnetic.

We return to He^+ implantation for a discussion of magnetic properties other than H_{un}. Figure 7 shows the values of $4\pi M$, A/M, H_1, and α versus maximum $\Delta\epsilon$. Due to poorer sensitivity, the profile shapes of $4\pi M$, A/M, H_1, and α cannot be independently determined. In the dose range below saturation of ΔH_{un}, a good fit is obtained if the implantation-induced changes are assumed proportional to $\Delta\epsilon$. The extreme variation then occurs at the point where the strain is a maximum. For higher doses the variations are less certain, particularly when a part of the surface layer becomes paramagnetic. A good fit is still obtained if the changes are proportional to $\Delta\epsilon$, except that $4\pi M$ and A/M go to 0 at $\Delta\epsilon \approx 2.3\%$ and remain 0 for higher strain.

The variation of H_1 is less certain but it clearly decreases as the strain increases. The bulk value, -165 ± 5 Oe, was determined with good accuracy by measuring the

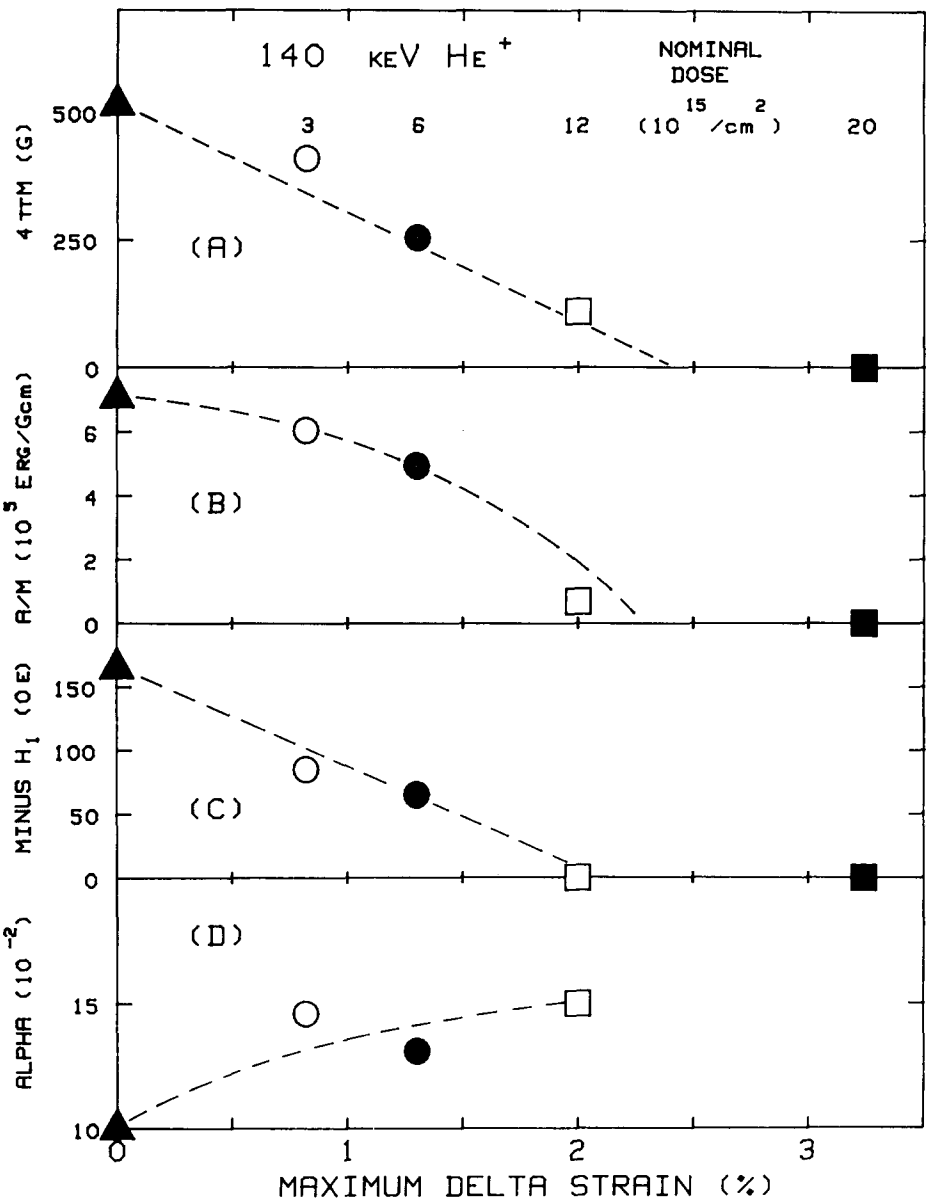

FIG. 7. Extremum values of magnetic properties vs $\Delta\epsilon_{max}$ for the four He^+ doses. Values obtained for each dose are represented by their own symbol. (a) Saturation magnetization $4\pi M$. (b) Ratio (A/M) of exchange stiffness constant to saturation magnetization. (c) Cubic anisotropy field H_1. (d) Damping coefficient α (note zero suppression).

bulk resonance mode as a function of angle. This procedure when applied to the surface modes can only be used to estimate the minimum value of H_1 since the large uniaxial anisotropy masks the effects of H_1 and since accurate analysis is not feasible for spin-wave resonance at angles other than parallel and perpendicular. The asymmetry of the resonance field for the principal surface mode versus angle suggests that H_1 decreases about 70% for the dose where $\Delta\epsilon = 1.3\%$. Comparison of perpendicular and parallel spectra requires a change nearly twice as large or else requires a small increase ($\sim 4\%$) in the surface value of γ (perpendicular and parallel FMR cannot distinguish between these parameters). The bulk value of γ is 1.503×10^7 (Oe sec)$^{-1}$. This is 15% lower than that of pure YIG, a feature attributed to the presence of rare earth ions. It is quite plausible that implantation damage would reduce this effect. The damping coefficient α is another parameter which increases with strain. At $\Delta\epsilon \simeq 2.3\%$, where most magnetic parameters go to 0, α reaches a value 50% larger than in the bulk. For $\Delta\epsilon > 2.3\%$ the material is paramagnetic and α is not defined.

As shown in Fig. 8, the magnetic properties of the Ne^+ implanted samples behave in a way that is similar to He^+ implantation. The major differences are the higher rate of decrease with strain and consequently the lower value of $\Delta\epsilon$ for which $4\pi M$, A/M, and H_1 go to 0 (1.8 vs 2.3%), and the large increase of α with $\Delta\epsilon$. As for helium implantation, the transition to paramagnetism is accompanied by a rapid drop in ΔH_{un} [Fig. 6(b)].

F. Discussion of magnetic properties for Ne^+ and He^+ implantation

We have seen that for both Ne^+ and He^+ implantation the parameters M and A which define garnet as ferrigmagnetic decrease with increasing strain (and damage) and that for a certain strain they go to 0. The local transition to paramagnetism occurs for damage levels roughly 30% below that required for amorphousness. The information obtained so

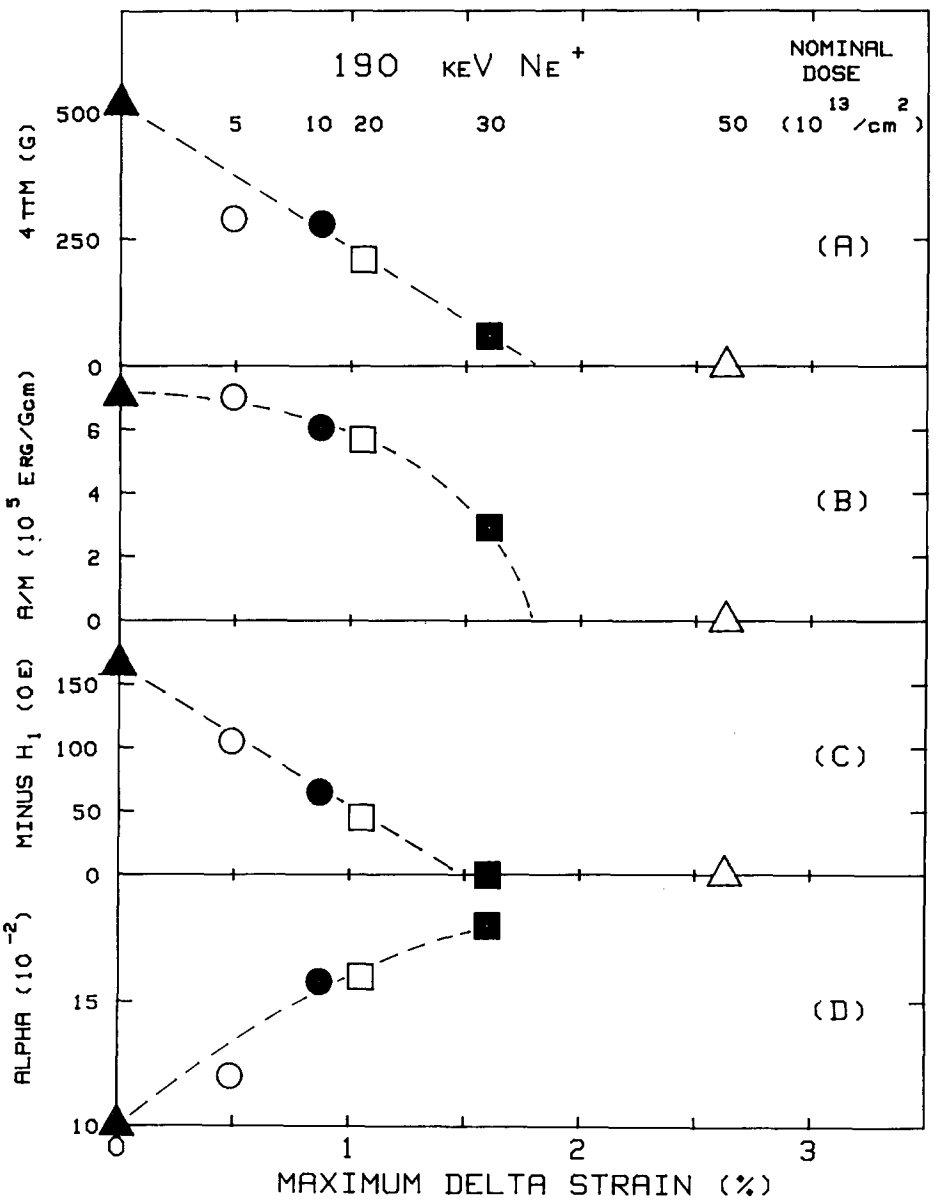

FIG. 8. Extremum values of magnetic properties vs $\Delta\epsilon_{max}$ for the five Ne^+ doses.

far is, of course, still insufficient to permit an identification of the source of the changes in magnetic properties. One is tempted to attribute the destruction of ferrimagnetism to incoherent atomic displacements. There is even a correspondence between the more rapid decrease in $4\pi M$ and A/M with strain on one hand and on the other hand the larger increase of damage with strain for neon versus helium implantation. However amorphous ferromagnetic materials do exist. It is conceivable that the large albeit coherent strains caused by implantation also contribute to the transition to paramagnetism. We can say very little about the increase in the damping parameter α with strain and damage. The increase implies larger losses from magnetic excitations to lattice vibration. In unimplanted doped YIG the losses are attributed to the presence of rare earth ions.[39] Their role in implanted doped YIG is poorly understood, since in Ref. 5 a large (400 Oe) virgin linewidth decreases while in the present case a low (70 Oe) virgin linewidth increases with damage.

Figures 6, 7, and 8 show that $-\Delta H_k$ is the dominant component of ΔH_{un}. The first important feature of the relation between ΔH_k and $\Delta\epsilon$ is the initial linearity and value of the slope which matches the estimated magnetostrictive effect. The component of bulk H_k attributable to growth-induced anisotropy is about 500 Oe whereas ΔH_k can be as large as 3000 Oe. There is therefore no evidence that at low doses the change in H_k is due to the suppression of growth-induced anisotropy.[43]

The second important feature is the saturation and decrease in ΔH_k with increasing $\Delta\epsilon$. This is similar to the reported saturation and decrease in stress in another garnet.[14,16] A detailed correlation of these separate experiments is not possible, but the source of the decrease in both cases might well be the same and is likely to be the damage. The ratio of ΔH_k to stress could in principle be used to define a parameter $3\lambda_{111}/M$, but it is unlikely that this would be the same parameter obtained by application of external stress and deformation to this same implanted material.

We do not have an explanation for the departure from a unique relation between ΔH_{un} and $\Delta\epsilon$ at high doses, but the sensitivity of the fitting procedure and the accuracy of the spectrum give us confidence that the difference is real.

It has been observed in Figs. 2(a) and 2(b) that from medium to high doses the separation in resonance field between principal surface and body mode is relatively insensitive to maximum strain and dose. This is a natural consequence of the saturation and decrease in ΔH_k with increasing strain. In $\perp$ FMR the principal surface mode is localized in the region neighboring the maximum H_{un}. At increasing doses this maximum does not change, but shifts location from the point of maximum strain towards the interface with unimplanted material, even after large portions of the implanted layer have become paramagnetic. This also indicates that the shift of this mode with external elastic deformation cannot be used to measure λ_{111}/M in the saturation region.

G. Magnetic profiles for H_2^+ implantation

The effects of H^+ implantation on ΔH_{un} are known to be markedly different from those of other ions. In a given material, for He^+, B^+, C^+, O^+, and Ne^+ implantation the separation $\Delta H_\perp$ between principal surface and body modes in $\perp$ FMR saturates with increasing dose at a value not exceeding 3 kOe.[44] In the same material, implantation with hydrogen causes $\Delta H_\perp$ to increase with dose beyond measurement capability at 10 GHz ($\Delta H_\perp \approx 10$ kOe). Conversely, for hydrogen implantation $\Delta H_\perp$ decreases rapidly with annealing temperature around 350 °C, while $\Delta H_\perp$ for other ions changes relatively little.[44] The rapid decrease in $\Delta H_\perp$ correlates with annealing-induced desorption of hydrogen.[8] Upon annealing up to 700 °C $\Delta H_\perp$ shows a nonlinear dependence on the strain.[10] Comparison of strain, magnetostriction constant and $\Delta H_\perp$ for deuterium implantation shows an excess contribution to ΔH_k which is not attributable to simple magnetostriction.[55] Even in garnets with very low λ_{111} large values of $\Delta H_\perp$ are observed.[46] These results strongly suggest chemical effects associated with the presence of implanted hydrogen. Our results support this view.

Figure 9(a) shows the distribution of ΔH_{un} as a function of depth obtained for 120 keV, $5\times10^{15}/cm^2$ H_2^+. This distribution corresponds to the third FMR spectrum of Fig. 2(c). The maximum ΔH_{un} is 4.5 kOe, a value greater than any obtained with Ne^+ or He^+ implantation. If the total ΔH_{un} profile is assumed to consist of a magnetostrictive contribution due to strain and a contribution due to a different mechanism, then a comparison with the strain profile may yield information about the unknown mechanism. Figure

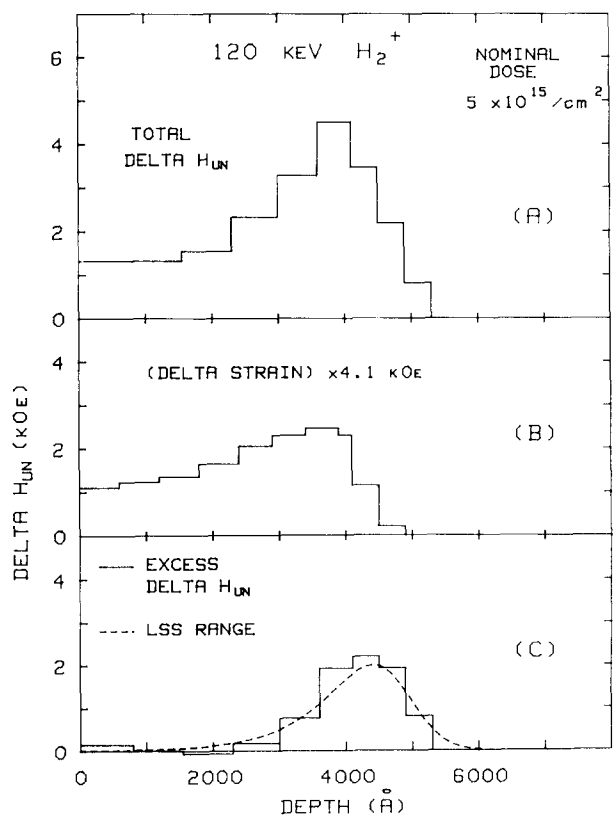

FIG. 9. Depth profiles of ΔH_{un} for 120 keV, $5\times10^{15}/cm^2$ H_2^+ implantation. (a) FMR-determined ΔH_{un} distribution. (b) $\Delta\epsilon$ profile multiplied by 4.1 kOe. (c) Difference between profiles (a) and (b). Also shown (dashed) is calculated LSS range of 60 keV H^+ in garnet.

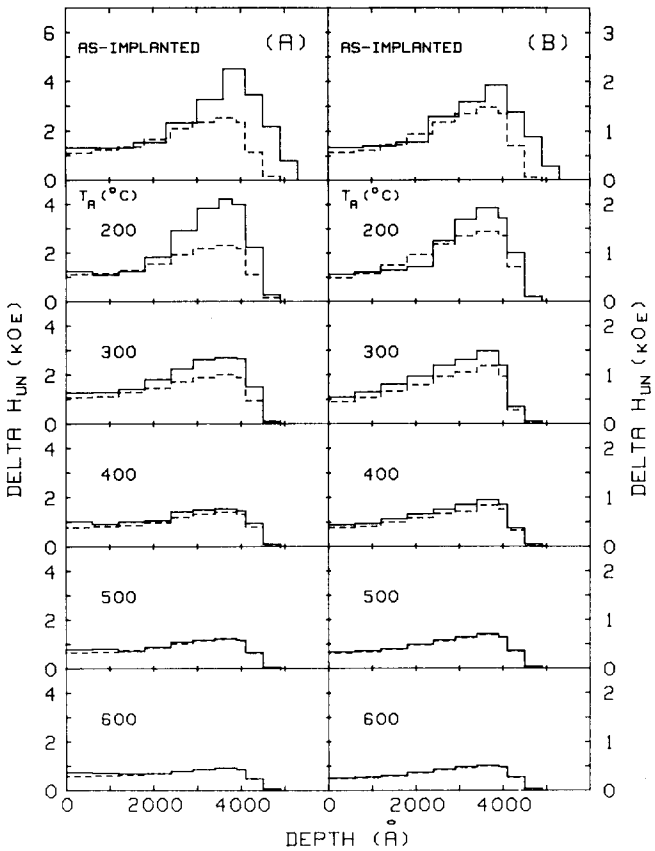

FIG. 10. (a) and (b), respectively, show total ΔH_{un} profiles (solid) and $\Delta\epsilon \times 4.1$ kOe profiles (dashed) for 5×10^{15}/cm^2 and 2×10^{15}/cm^2 120 keV H_2^+ implantation. Profiles are for successively higher annealing temperature. Note the different vertical scales.

9(b) shows the strain distribution multiplied by 4.1 kOe/%. Since the maximum $\Delta\epsilon$ for this case is only 0.60%, it is reasonable to assume that the initial linear relation between ΔH_{un} and $\Delta\epsilon$ found for Ne^+ and He^+ is also valid here. Figure 9(c) shows the difference between total and magnetostrictive ΔH_{un}. The excess ΔH_{un} is in remarkable agreement with the calculated LSS range (the local density of hydrogen atoms). This agreement strongly suggests a connection between ΔH_{un} and the presence of hydrogen. The connection is further confirmed by comparing the profiles of ΔH_{un} and $\Delta\epsilon$ before and after annealing at successively higher temperatures. Figures 10(a) and 10(b) show such a sequence for nominal doses 5×10^{15}/cm^2 and 2×10^{15}/cm^2, respectively. Before annealing the ratio of maximum ΔH_{un} to maximum $\Delta\epsilon$ is greater for the sample with higher dose, indicating that the excess ΔH_{un} increases more rapidly with dose than does $\Delta\epsilon$. With annealing below 400 °C the excess ΔH_{un} shifts toward the location of maximum strain and damage and decreases with increasing temperature. Gettering of implanted dopants from regions with low damage to regions with higher damage has been reported for other materials.[57] The diminishing amount of excess ΔH_{un} is consistent with the desorption of hydrogen at these temperatures. After annealing at 400 °C, little or no hydrogen remains in the crystal[8] and the total ΔH_{un} coincides with the contribution due to strain. Annealing at 500 and 600 °C decreases ΔH_{un} and $\Delta\epsilon$ but maintains the magnetostrictive relation.

In addition to the unusual effect on ΔH_{un} which is primarily a change in uniaxial anisotropy, hydrogen implantation also causes unusual changes in $4\pi M$, A/M and α. For the case shown in Fig. 9, where the maximum $\Delta\epsilon$ is only 0.60%, there is a 60% reduction in $4\pi M$. If the same maximum strain is obtained with Ne^+ or He^+, the reduction is less than 30%. For hydrogen implantation the region with significantly lowered $4\pi M$ extends beyond the strained layer up to the depth of excess ΔH_{un}. For Ne^+ and He^+ implantation the decrease in $4\pi M$ is accompanied by a decrease in A/M. For hydrogen the exchange constant decreases more slowly than $4\pi M$, resulting in an increase in A/M. For the distribution of Fig. 9, the average A/M is 43% greater than bulk value. This is accompanied by an increase of a factor of two in α.

As in the case of Ne^+ and He^+, we have limited understanding of what causes the changes in magnetic properties for hydrogen implantation. The reduction in magnetization accompanied by a smaller reduction in A suggests that incoherent atomic displacements play a smaller role than for Ne^+ and He^+, and the profiles support the view that the presence of hydrogen atoms is a significant factor. The same appears to be true of H_k, but the uniaxial character is intriguing.

It would be informative to do detailed x-ray and FMR analyses of deuterium implanted garnet. Since for deuterium nuclear stopping is greater than for hydrogen, the relative contribution of the strain compared to the contribution attributable to chemistry would be greater. Published results already show that for deuterium ΔH_{un} is greater than expected from simple magnetostriction.[55]

The discovery of large chemical effects for hydrogen implies that other ions may also produce effects not associated with strain or damage. But if detectable chemical effects require dopant concentrations of at least 1%, such measurements are difficult. For all other ions the implanted garnet is rendered paramagnetic with doses yielding concentrations well below 1%.

H. Results of annealing

In this paper the study of annealing behavior was limited to the two lower doses of Ne^+ and He^+ implantation and to the three lower doses of H_2^+ implantation. For Ne^+ and He^+ at these doses the relationships between ΔH_{un} and $\Delta\epsilon$ are independent of depth and consequently FMR spectra are easily interpreted. The maximum strain and ΔH_{un} for the lowest dose hydrogen implantation were too low after annealing to provide significant quantitative information. The reasons for excluding the high-dose hydrogen implantations were discussed earlier.

For all three species the strain decreases with increasing annealing temperature. However the changes in profile shape are negligible. For each species it is thus possible to normalize the profiles to the profile obtained prior to annealing. Figure 11 shows the results. It is worth noting that before annealing and normalizing the maximum values of $\Delta\epsilon$ were 0.49 and 0.87% for Ne^+; 0.82 and 1.30% for He^+; and 0.35 and 0.60% for H_2^+. For Ne^+ and H_2^+ the annealing

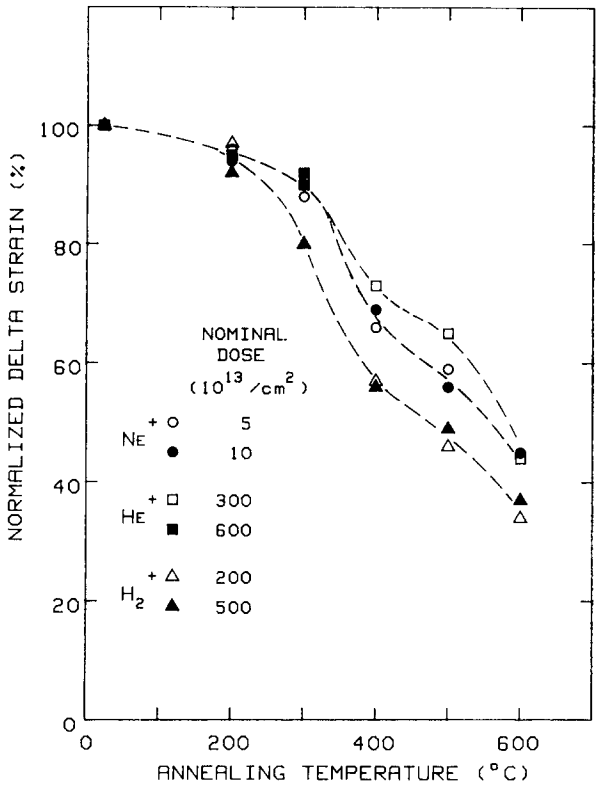

FIG. 11. Normalized strain $\Delta\epsilon$ vs annealing temperature for neon, helium and hydrogen implantation.

behavior is nearly independent of the magnitude of the original strain. For He^+ implantation at $6\times10^{15}/cm^2$ annealing at $\sim$400 °C results in severe broadening of both x-ray and FMR spectra. At this and higher doses there is a formation of He bubbles[24,5] which results in a deterioration of crystalline and magnetic properties. The present measurements on the lower doses of He^+ implantation did not show any broadening up to 600 °C.

Although the strain for hydrogen decreases more rapidly with annealing temperature than the strain for neon and helium, the general trend is the same for all three species. This reinforces the idea that despite the large differences in dose, the major source of the strain is independent of ion species. The more rapid decrease of strain for temperatures between 300 and 400 °C and again between 500 and 600 °C has been previously reported for Ne^+ implantation.[12] The present measurements and all other measurements known to us do not provide information permitting speculation concerning the reasons for this behavior. For all six cases and especially after annealing the damage is too low for meaningful measurement.

The behavior of magnetic properties for Ne^+ and He^+ implantation is reasonably consistent with the strain. As the strain decreases, the profiles of ΔH_{un} follow the curves of Figs. 6(a) and 6(b). Slight inconsistencies are observed for $4\pi M$ and A/M. The magnetization increases with annealing, reaching its bulk value at 600 °C, where the strain has relaxed only half way. For both species the ratio of A/M also increases with annealing but at 600 °C remains some 20% below bulk value. The damping parameter α decreases with annealing, reaching the bulk value around 400 °C, and for higher temperature it drops 10% below this value. The cubic anisotropy remains 20 to 50% low after annealing up to 400 °C. We have already shown the annealing behavior of ΔH_{un} for hydrogen implantation. In this case the values of $4\pi M, A/M$ and α also move toward and reach the respective bulk values at 600 °C.

VI. CONCLUDING REMARKS

It has been shown that a considerable amount of information can be obtained by combining detailed analyses of x-ray and FMR spectra of ion-implanted garnet. Several conclusions afforded by detailed analysis are substantially different from conclusions based only on considerations of $\Delta H_\perp$, the separation of principal surface mode and bulk mode in FMR and on the maximum extent $\Delta\theta$ of the rocking curve in x-ray diffraction. Some of the results clarify various aspects of implanted garnet; other results raise new and difficult questions. The major feature to be explained is the departure at high doses from a unique relationship between ΔH_{un} and $\Delta\epsilon$. Also, a study of the annealing behavior of samples implanted at high dose would be worthwhile.

An important question is whether or not the present results are specific to the garnet and the implanted species used. This cannot be clearly answered due to the lack of a theory of the properties of implanted garnet. Nevertheless it is probable that the general features of the present results are reproduced in all magnetic garnets implanted with a variety of ion species. Judging by published x-ray rocking curves, the strain depends on ion species, energy, dose and annealing but is insensitive to the composition of the garnet. Regardless of implanted species, all garnets are probably rendered amorphous at strains around 3%. Complete and detailed FMR spectra of implanted garnet have been rarely published, but the more frequently published dependence of $\Delta H_\perp$ on ion species, dose, etc., is similar to our observations. We infer that the entire structures of these spectra are also similar to the present measurements. Thus we expect that magnetic profiles of garnets with different compositions and implanted with different ions are similar to those of the films we have studied.

ACKNOWLEDGMENTS

One of the authors (VSS) thanks the International Business Machines Corporation for financial support in the form of a predoctoral fellowship. We thank Tim Gallagher, Kochan Ju, H. Ben Hu, and Chris Bajorek of the San Jose laboratory of IBM for supplying the samples and encouraging this study. We express appreciation to Lavada Moudy, Howard Glass, and Jack Mee of Rockwell International (Anaheim, California) for providing easy access to a double-crystal diffractometer. We thank Jim Campbell of Caltech for suggesting the use of and providing us with the HP 9826 computer. Thad Vreeland of Caltech encouraged us to accept an unusual x-ray result.

[1] J. C. North and R. Wolfe, "Ion-Implantation Effects in Bubble Garnets" in *Ion-Implantation in Semiconductors and Other Materials*, edited by B. L. Crowder (Plenum, New York, 1973).

[2]K. Komenou, I. Hirai, K. Asama, and M. Sakai, J. Appl. Phys. **49**, 5816 (1978).
[3]V. S. Speriosu, H. L. Glass, and T. Kobayashi, Appl. Phys. Lett. **34**, 539 (1979).
[4]H. Jouve, P. Gerard, A. Luc, IEEE, Trans. Magn. **MAG-16**, 946 (1980).
[5]V. S. Speriosu, B. E. MacNeal, and H. L. Glass, Intermag 1980 Conference, Boston, paper 22-4 (unpublished).
[6]W. de Roode and J. W. Smits, J. Appl. Phys. **52**, 3969 (1981).
[7]V. S. Speriosu, J. Appl. Phys. **52**, 6094 (1981).
[8]Y. Sugita, T. Takeuchi, and N. Ohta, Magnetism and Magnetic Materials Conference, 1981, Atlanta, Paper CA-5 (unpublished).
[9]Y. Satoh, M. Ohashi, T. Miyashita, and K. Komenou, J. Appl. Phys. **53**, 3740 (1982).
[10]G. Suran, H. Jouve, and P. Gerard, J. Appl. Phys. **54**, 2006 (1983).
[11]V. S. Speriosu and C. H. Wilts, Magnetism and Magnetic Materials Conference 1981, Atlanta, Paper BA-9 (unpublished).
[12]W. H. de Roode and H. A. Algra, J. Appl. Phys. **53**, 2507 (1982).
[13]H. A. Algra and W. H. de Roode, J. Appl. Phys. **53**, 5131 (1982).
[14]H. Jouve, J. Appl. Phys. **50**, 2246 (1979).
[15]T. J. Nelson, R. Wolfe, S. L. Blank, and W. A. Johnson, J. Appl. Phys. **50**, 2261 (1979).
[16]J. P. Kersusan, P. Gerard, J. P. Gailliard, and H. Jouve, IEEE Trans. Magn. **MAG-17**, 2917 (1981).
[17]W. A. Johnson, J. C. North, and R. Wolfe, J. Appl. Phys. **44**, 4753 (1973).
[18]H. A. Washburn and G. Galli, J. Appl. Phys. **50**, 2267 (1979).
[19]H. Jouve and M. T. Delaye, IEEE Trans. Magn. **MAG-16**, 949 (1980).
[20]P. Gerard, M. T. Delaye, and R. Danielou, Thin Solid Films **88**, 75 (1982).
[21]P. Gerard, P. Martin, and R. Danielou (to be published).
[22]B. M. Paine, V. S. Speriosu, L. S. Wielunski, H. L. Glass, and M-A. Nicolet, Nucl. Instrum. Methods **191**, 80 (1981).
[23]T. Omi, C. L. Bauer, and M. H. Kryder, J. Appl. Phys. **53**, 2528 (1982).
[24]R. Wolfe, J. C. North, and Y. P. Lai, Appl. Phys. Lett. **22**, 683 (1973).
[25]R. F. Soohoo, J. Appl. Phys. **49**, 1582 (1978).
[26]J. P. Omagio and P. E. Wigen, J. Appl. Phys. **50**, 2264, (1979).
[27]C. H. Wilts, J. Zebrowski, and K. Komenou, J. Appl. Phys. **50**, 5878 (1979).
[28]K. Komenou, J. Zebrowski, and C. H. Wilts, J. Appl. Phys. **50**, 5442 (1979).
[29]H. A. Algra and J. M. Robertson, J. Appl. Phys. **51**, 3821 (1980).
[30]J. Mada and K. Asama, J. Appl. Phys. **50**, 5914, (1979).
[31]C. H. Wilts and S. Prasad, IEEE Trans. Magn. **Mag-17**, 2405 (1981).
[32]G. Suran, R. Krishnan, P. Gerard, and H. Jouve, IEEE Trans. Magn. **MAG-17**,. 2920 (1981).
[33]I. Maartense and C. W. Searle, Appl. Phys. Lett. **34**, 115 (1979).
[34]P. H. Smit, H. A. Algra, and J. M. Robertson, Appl. Phys. **22**, 299 (1980).
[35]A. H. Morrish, P. J. Picone, and N. Saegusa, to be published in J. Magn. Magn. Mater.
[36]R. Krishnan, S. Visnovski, V. Prosser, and P. Gerard, IEEE Trans. Magn. **MAG-18**, 1280 (1982).
[37]K. Ju, R. O. Schwenker, and H. L. Hu, IEEE Trans. Magn. **MAG-15**, 1658 (1979).
[38]B. E. MacNeal and V. S. Speriosu, J. Appl. Phys. **52**, 3935 (1981).
[39]See for example, P. Hansen, "Magnetic anisotropy and magnetostriction in garnets", in *Physics of Magnetic Garnets*, edited by A. Paoletti (North-Holland, New York, 1978).
[40]B. Hoekstra, F. Van Doveren, and J. M. Robertson, Appl. Phys. **12**, 261 (1977).
[41]G. P. Vella-Coleiro, Rev. Sci. Instrum. **50**, 1130 (1979).
[42]X. Wang, C. S. Krafft, and M. H. Kryder, to be published in J. Magn. Magn. Mater.
[43]G. P. Vella-Coleiro, R. Wolfe, S. L. Blank, R. Caruso, T. J. Nelson, and V. V. S. Rana, J. Appl. Phys. **52**, 2355 (1981).
[44]R. Hirko and K. Ju, IEEE Trans. Magn. **MAG-16**, 958 (1980).
[45]H. Matsutera, S. Esho, and Y. Hidaka, J. Appl. Phys. **53**, 2504 (1982).
[46]H. Makino, Y. Hidaka, and H. Matsutera, to be published in J. Magn. Magn. Mater.
[47]San Jose, California, Laboratory of IBM.
[48]See for example, J. W. Mayer, L. Eriksson, and John A. Davies, *Ion Implantation in Semiconductors* (Academic, New York, 1970).
[49]V. S. Speriosu, B. M. Paine, M-A. Nicolet, and H. L. Glass, Appl. Phys. Lett. **40**, 604 (1982).
[50]G. A. Rozgonyi, P. M. Petroff, and M. B. Panish, Appl. Phys. Lett. **24**, 251 (1974).
[51]See for example, W. H. Zachariasen, *Theory of X-ray Diffraction in Crystals* (Wiley, New York, 1945).
[52]C. H. Wilts, Magnetism and Magnetic Materials Conference 1981, Atlanta, paper CA-6. (unpublished).
[53]J. F. Gibbons, W. S. Johnson, and S. W. Mylroie, *Projected Range Statistics*, 2nd ed. (Halstead, New York, 1975).
[54]R. D. Pierce, R. Caruso, and C. J. Mogab, J. Appl. Phys. **53**, 4480 (1982).
[55]A. M. Guzman, C. S. Krafft, X. Wang, and M. H. Kryder, to be published in Nucl. Instrum. Methods.
[56]W. L. Johnson (verbal communication).
[57]See for example, R. G. Wilson and D. M. Jamba, Electrochemical Society Meeting, Denver, 1981, abstract 333.